nature reviews chemistry

https://doi.org/10.1038/s41570-025-00702-w

Review article

Check for updates

Multifaceted nature of defect tolerance in halide perovskites and emerging semiconductors

Irea Mosquera-Lois [1,3], Yi-Teng Huang [2,3], Hugh Lohan [1,2,3], Junzhi Ye [2], Aron Walsh [1] ✉ & Robert L. Z. Hoye [2] ✉

Abstract

Lead halide perovskites (LHPs) have shot to prominence as efficient energy-conversion materials that can be processed using cost-effective fabrication methods. A reason for their exceptional performance is their crystallographic defect tolerance, enabling long charge-carrier lifetimes despite high defect densities. Achieving defect tolerance in broader classes of materials would impact on the semiconductor industry substantially. Considerable efforts have been made to understand the origins of defect tolerance, so as to design stable and nontoxic alternatives to LHPs. However, understanding defect tolerance in LHPs is far from straightforward. This Review discusses the models proposed for defect tolerance in halide perovskites, evaluating the experimental and theoretical support for these models, as well as their limitations. We also cover attempts to apply these models to identify materials beyond LHPs that could exhibit defect tolerance. Finally, we discuss the experimental methods used to understand defects in mixed ionic–electronic conductors, as well as the important information that is necessary for a deeper understanding, in order to develop improved models that enable the design of defect-tolerant semiconductors.

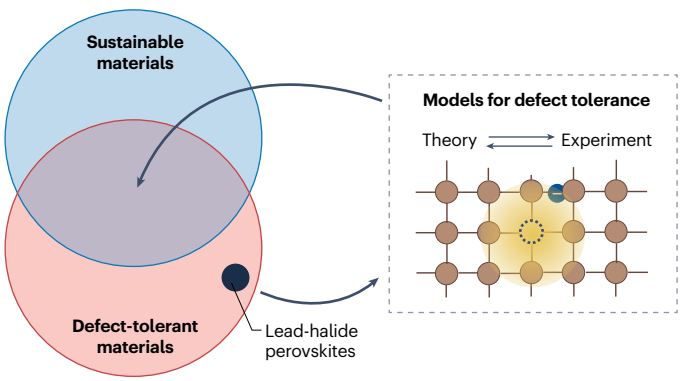

Sections

[1]Department of Materials, Imperial College London, London, UK. [2]Inorganic Chemistry Laboratory, Department of Chemistry, University of Oxford, Oxford, UK. [3]These authors contributed equally: Irea Mosquera-Lois, Yi-Teng Huang, Hugh Lohan. ✉e-mail: a.walsh@imperial.ac.uk; robert.hoye@chem.ox.ac.uk

Introduction

Semiconductors that harvest light to produce clean electricity[1,2] or clean fuels and chemicals[3–5], without emitting any greenhouse gases, are becoming increasingly important for enabling society's transition towards net-zero carbon dioxide-equivalent emissions. The deployment of these technologies benefits from cost-effective manufacturing methods, but implementing these methods typically leads to a compromise in performance because of the deleterious role played by defects[1]. Defects in semiconductors lower the performance by causing irreversible losses in energy (see Box 1), as well as limiting the transport of charge carriers. The effects of defects have traditionally been mitigated by minimizing their presence through careful growth and the passivation of materials[1,2,6,7]. However, since the 2010s, lead halide perovskites (LHPs) have proven to be an exception, rapidly rising in performance in photovoltaics (Fig. 1a), which harvest light to produce clean electricity. The most efficient LHP photovoltaic devices are made using simple solution processing or evaporation methods; they are polycrystalline, and the absorber layer is processed at temperatures up to only 150 °C[8]. By contrast, the most efficient Si photovoltaics are made using capital-intensive equipment, they are single-crystalline, and they are processed at >1,000 °C; yet, the certified record light-to-electricity power conversion efficiencies (PCEs) are very similar (27.3% for Si photovoltaics and 27.0% for LHP photovoltaics, at present)[8,9]. The ability to achieve efficient LHPs using standard laboratory equipment has engaged a large global community, such that the cycles of learning required to reach the performance of single-crystalline Si photovoltaics have taken a considerably shorter period of time than for other materials, according to the National Renewable Energy Laboratory[10,11] (see Fig. 1a,b).

This unusual high performance of LHPs has largely been attributed to defect tolerance, according to which high PCEs are achievable in solar cells despite a high defect density by primarily forming defects that do not promote free carrier recombination (for example, with low rate-limiting capture coefficients, as shown in Fig. 1c)[6,7,12–15]. Indeed, photovoltaics based on polycrystalline LHP thin films can achieve 21.2% PCE without any dedicated efforts to intentionally passivate defects in the bulk of the perovskite layer or at interfaces[16], reaching 69% of the maximum theoretical efficiency predicted by the Shockley–Queisser model[16,17] (Fig. 1d). By contrast, polycrystalline Si photovoltaics only reach ~17% PCE without substantial interface passivation[18–20] (Fig. 1d). If we compare LHPs with another polycrystalline direct-bandgap material, CdTe photovoltaics only reach ~10% PCE without passivation[21,22], whereas the optimally passivated devices are at only 70% of the theoretical limit — in contrast with the value of 80% for passivated LHPs (Fig. 1d). Even in the most efficient LHP photovoltaics, the defect density (10^{13}–10^{17} cm^{-3}; or parts per billion to parts per million)[23–26] is orders of magnitude larger than in optimized single-crystalline Si (<10^{11} cm^{-3} — in other words, parts per quadrillion or lower)[27].

Defect tolerance in solar absorbers was discussed before the turn of the century by Zhang et al. to account for the surprisingly high efficiency of $CuInSe_2$, despite hosting extraordinarily high concentrations of native defects, on the order of ~1%[28]. In this case, defect tolerance arises because the deep indium on copper antisites (In_{Cu}^{2+}) and copper vacancies (V_{Cu}^{-}) combine to form benign complexes ($2V_{Cu}^{-} + In_{Cu}^{2+}$) that can order to form new crystallographic phases[28]. However, for LHPs, a wide range of models have been put forward to account for their tolerance towards point defects, which draw upon electronic and structural factors[29–31]. The concept of defect tolerance has been extended by considering that dynamic disorder of LHPs results in substantial energetic fluctuations in trap levels, by as much as 1 eV on a ps timescale[32], raising the question of how traps can be considered shallow or deep. Defect spectroscopy in LHPs is also complicated by contributions from ionic and electronic processes, which are difficult to disentangle[33]. Deep-level transient spectroscopy (DLTS) measurements have indicated the presence of deep traps[34,35]. Some of these defects are relatively benign, with small capture cross-sections (~10^{-15} cm^2)[34,35], whereas other works have identified more harmful defects with larger capture cross-sections ~10^{-12} cm^2 (ref. 35). Using positron annihilation lifetime spectroscopy (PALS) on methylammonium lead iodide ($MAPbI_3$), negatively charged Pb vacancies were identified and found to act as recombination centres[36]. The concentration of these V_{Pb}^{2-} was estimated to be high, in the 10^{15}–10^{17} cm^{-3} range[36]. Despite this, the non-radiative recombination coefficient reported for $MAPbI_3$ ($1.4–1.5\times10^7$ s^{-1}) is similar to established inorganic semiconductors, such as single-crystalline Si ($0.1–2.5\times10^7$ s^{-1}) and GaN ($0.1–1.0\times10^7$ s^{-1})[37].

The field has therefore reached a critical juncture, in which it is important to bring together the experimental and computational work, especially those made since the 2010s, to evaluate the multifaceted nature of defect tolerance in LHPs. This Review begins by discussing the definition of defect tolerance, which is inconsistent between communities because of the different ways in which defects are probed. Next, we evaluate the models put forward for defect tolerance, discussing the evidence for and against these models. We balance out the Review with a discussion of efforts to generalize defect tolerance beyond LHPs, which can lead to the discovery of efficient and cost-effective solar absorbers that overcome the stability and toxicity limitations of halide perovskites. We discuss the strategies that have been adopted, as well as the successes and challenges found among the materials investigated. Furthermore, we discuss the challenges of experimentally probing defects, as well as some of the improved spectroscopy and microscopy techniques developed. We finish off with a discussion of some of the important questions that need to be addressed to move forward towards a consolidated view of defect tolerance and the development of design rules that enable the discovery of defect-tolerant semiconductors.

Defect tolerance in halide perovskites

In this section, we discuss how views around the definition of defect tolerance have evolved over time, the roles that defects over different length scales play, and the models that have been put forward for explaining how defect tolerance comes about in LHPs.

Defining defect tolerance

A specific and widely accepted definition of defect tolerance remains elusive, partly because of continued debate over how defect tolerance arises and partly because of the different probes used for evaluating the role of defects — from computational methods (Box 2) to experimental techniques, and with sensitivities ranging from the parts per trillion up to the percent level (Box 3). Adding to these difficulties, not all defects detected from measurements are recombination-active. Analysing defect concentrations alone without understanding what these species are makes it challenging to relate to non-radiative recombination rates.

Zakutayev et al. defined defect tolerance as "the tendency of a semiconductor to keep its properties despite the presence of crystallographic defects"[31]. Brandt et al. subsequently built upon this to specify that materials could be defect-tolerant if they form low defect concentrations despite being processed rapidly at low temperature, or have minimal reductions in charge-carrier mobilities and

Box 1 | Charge-carrier trapping at defect sites

Point defects can create localized energy levels in crystalline materials. If these occur within the bandgap of a semiconductor, the associated charge transition levels (called traps) can capture electrons (e^-) and/or holes (h^+), resulting in charge-carrier annihilation that occurs without emitting photons (that is, non-radiative recombination). Photoexcitation leads to the introduction of excess carrier density with e^- in the conduction band and h^+ in the valence band. The rate of charge trapping by defects will depend on this excess carrier density (Δn), along with both the concentration of active defects (N_{defect}) and their capture coefficients (C_{defect}), as shown in the left diagram below.

The microscopic process that determines C_{defect} can be visualized with a configuration coordinate diagram (sketched below, right panel), in which each curve represents the energy of the system (E) as atoms are distorted from their equilibrium configuration (Q)[37,234]. Starting with a neutral defect (X^0) in the presence of excess charge carriers following photoexcitation (blue curve), by overcoming or tunnelling through the energy barrier E_b^n, an electron is captured, leading to a change in the defect charge state and distorting the local structure (change in Q). The system becomes a negatively charged defect with excess h^+ (red curve). Further overcoming energy barrier, E_b^p, leads to h^+ being captured by X^-, and the system re-entering the ground state (green curve). During this cycle, the energy of an electron and hole (that is, the bandgap, E_g) has been converted into heat through multi-phonon emission.

The overall non-radiative recombination rate depends on the carrier with the lowest capture rate, as described by the Shockley–Read–Hall model[235]. It is possible to obtain a low rate despite a high defect density by having traps close to one of the band-edges, such that the capture rate of one charge carrier is minimized (Fig. 1c). These are called shallow traps, and they are one route to defect tolerance. Although standard analysis for conventional semiconductors typically considers the regime of weak distortion (small changes in Q) and harmonic potential energy surfaces (such as parabolic E–Q curves), many defect charge transitions result in considerable rearrangements in bonding (for example, dimer formation), especially for materials with soft structures. In this case, the energy gap between the trap level and band extrema is a poor proxy for charge-carrier capture, requiring consideration of the full potential energy surface[236].

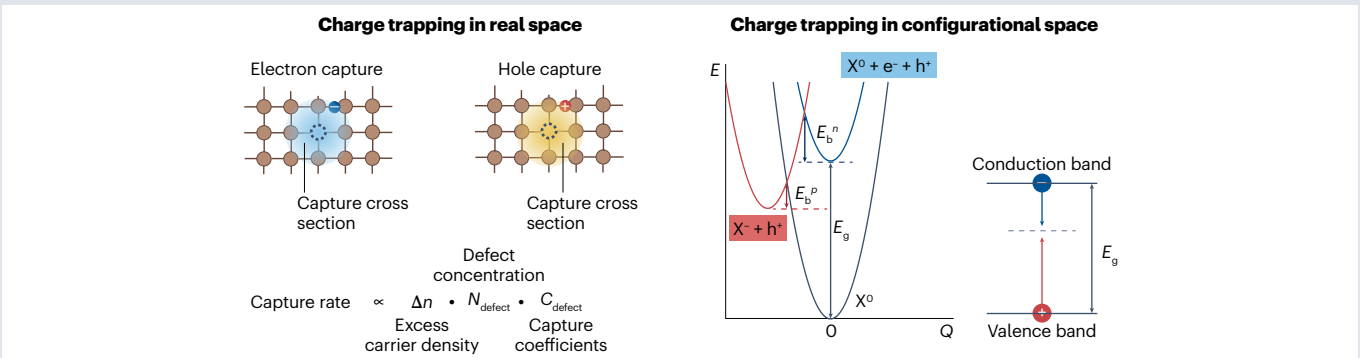

minority-carrier lifetimes, despite the presence of extrinsic, intrinsic or structural defects[30]. The definition of materials with defect tolerance as materials that have minimal reductions in charge-carrier mobilities and minority-carrier lifetimes, despite the presence of extrinsic, intrinsic or structural defects, recognizes the importance of long minority-carrier diffusion lengths to achieve efficient performance and that charge-carrier transport has historically limited the development of emerging thin-film solar absorbers[38]. It remains challenging to quantify 'minimal reductions', but for the purposes of materials screening, Buonassisi and co-workers proposed to use 1 ns minority-carrier lifetime as a critical threshold, given that established thin-film solar absorbers needed lifetimes exceeding this to eventually reach 10% PCE in photovoltaics[38,39]. However, it is difficult to directly compare the lifetimes between materials if their recombination processes are not identical due to the differing dependences on excess carrier density by trap-mediated, radiative and Auger recombination[39,40]. Furthermore, recombination rates depend on the excess carrier density, doping level and distribution of traps (whether they are mainly shallow or deep, or a mixture of both). Accurately determining lifetimes can therefore be challenging[41–43], especially for novel materials for which the nature of charge carriers and recombination mechanisms are not well established. Overly relying on minority-carrier lifetimes can also be deceptive if self-trapped excitons or small polarons form, which can lead to prolonged decays in the measured photoexcited charge-carrier population, but give substantial reductions in mobilities, thus overall leading to short diffusion lengths[44–46]. We therefore propose to refine this definition to 'the effect in which a semiconductor, which readily forms free carriers, does not experience a substantial increase in its non-radiative recombination rate or reduction in charge-carrier mobilities when defects are present in high concentrations', as materials with carrier localization, or which cannot readily separate excitons into free carriers, are inherently limited in performance. One way in which this manifests is if the defects present in semiconductors have low total capture coefficients (C_{defect}; Fig. 1c and Box 1). In this case, defect tolerance is not a binary property but rather a continuous one. Defect tolerance can also be manifest through self-healing (see section on this topic later in the Review), or defects pairing up to form benign defect complexes[28]. That being said, we cannot compare materials based on the values of C_{defect} due to a lack of available data, as calculating these values is computationally expensive and challenging to perform reliably for

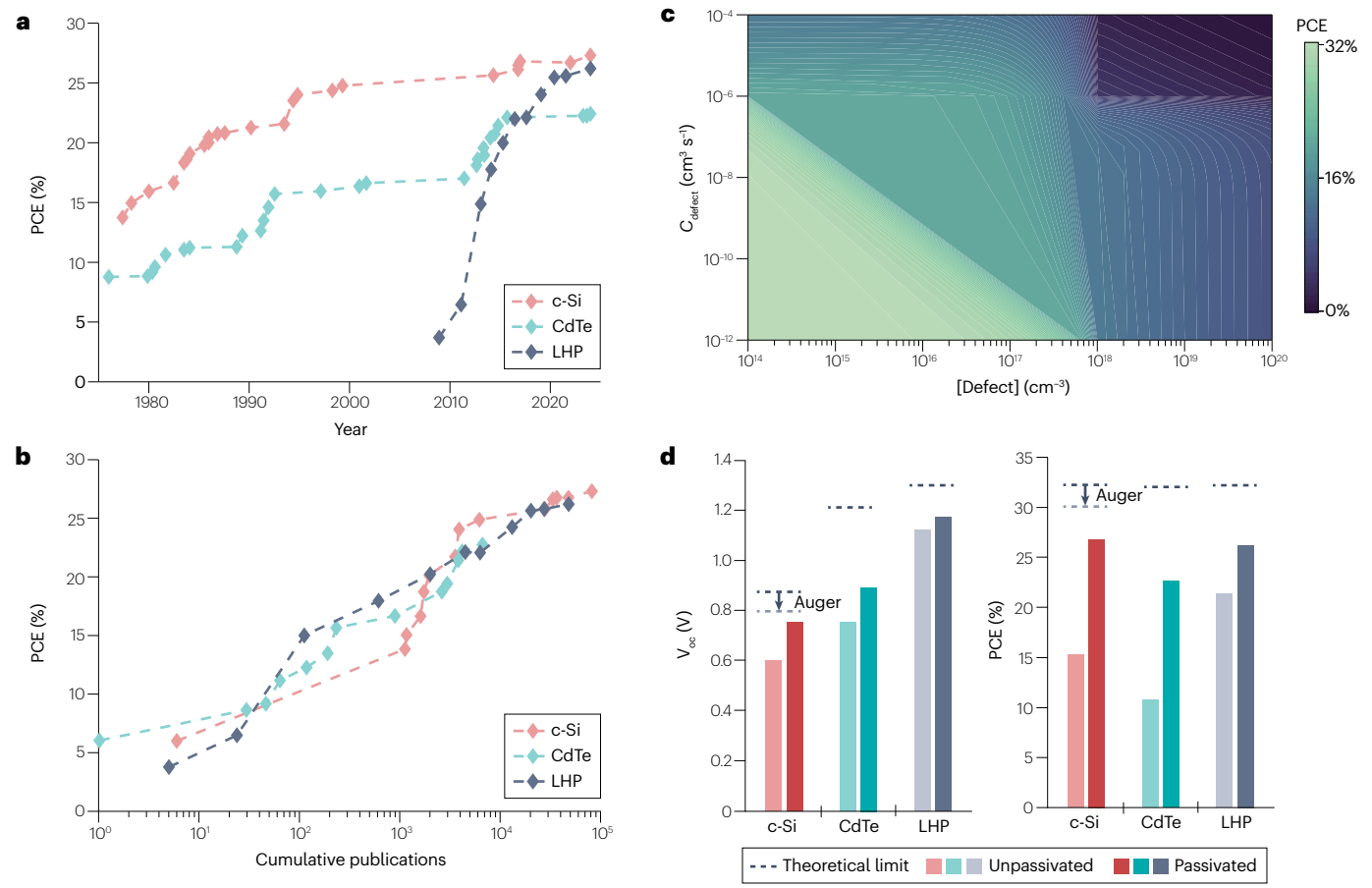

Fig. 1 | Impact of defect tolerance on the performance of solar absorbers. Comparison of the learning rate of lead halide perovskite (LHP) versus crystalline silicon (c-Si) and cadmium telluride (CdTe) photovoltaics, with respect to development time (part **a**) and cumulative number of publications (part **b**)[10,11,22], which can be considered as a proxy for the level of effort. **c**, Map of the theoretical maximum power conversion efficiency (PCE) of materials in photovoltaics, depending on the capture coefficient (C_{defect}) and concentration ([Defect]) of defects. **d**, Loss in open-circuit voltage (V_{OC}) and PCE of unpassivated and optimally passivated LHP, c-Si and CdTe photovoltaic devices compared with the radiative limit. The label Auger indicates the voltage loss due to non-radiative Auger recombination. PCE, power conversion efficiency.

halide perovskites, and it is difficult to determine C_{defect} experimentally from the recombination coefficient and defect concentration, due to difficulties in reliably measuring the concentration of a specific defect (Box 3). We suggest that, in the future, more emphasis could be placed on the photoluminescence quantum yield (PLQY), which can be measured without having to know or assume knowledge of the doping level, injection level or recombination mechanism (unlike extracting lifetimes[41,47]). However, many novel materials with indirect bandgaps have low PLQYs that are difficult to quantify above the noise level during the early stages of development, and there is no consensus on a cut-off in PLQY for a material to be considered promising for further development in photovoltaics[48].

Classifying the role of defects

A wide range of defect types exist in materials. These can be classified based on their scale and dimensionality. At the atomic scale, there are 0-dimensional (or 0D) point defects, comprised of one atom missing or misplaced (for example, vacancy, anti-site or interstitial). There are also structural defects, including 1D dislocations, 2D stacking faults and grain boundaries, and 3D twin domains, along with macroscopic voids, and defects occurring at surfaces and interfaces. Structural defects could be minimized through careful materials processing (for instance by increasing grain size or passivating surfaces), but 0D point defects are thermodynamically unavoidable, and they are also the most straightforward to model (Box 2). The discussion of defect tolerance has therefore focused on the effects of intrinsic point defects, and materials that tolerate point defects could also be more resilient to non-radiative recombination at structural defects. Indeed, this resilience has been observed for single-crystal LHPs, in which the optoelectronic properties seem unaffected by the presence of structural defects[49].

The presence of a defect does not necessarily lead to an increase in non-radiative recombination. Defects must capture both an electron and hole to annihilate them. The role of defects in optoelectronic materials, therefore, strongly depends on the capture rates for charge carriers, and this depends on the trap level and capture cross-section (Box 1), which describes the area around a defect where charge carriers can be captured, typically in the 10^{-4}–10^{4} Å^2 range[50,51]. Defects that do not introduce a trap level in the bandgap are recombination-inactive and are

therefore classified as benign defects (for example, V_I^+ in $CH_3NH_3PbI_3$)[52]. Such defects can give rise to defect tolerance, although they may be active in other ways, such as ion diffusion or chemical degradation. Similarly, defects with trap levels close to one of the band edges and low capture-cross-sections are not recombination-active (Box 1), but they will act as electron traps (close to conduction band minimum) or hole traps (close to valence band maximum), with very low capture rates for the other charge carrier. Recombination-active defects (termed recombination centres) tend to be defects with trap levels close to mid-gap, with similar capture coefficients for both charge carriers, especially if the capture coefficients are high. Such 'killer defects' can be detrimental even in low concentrations and include V_{Se} in Sb_2Se_3 (ref. 53) and V_S in Cu_2ZnSnS_4 (ref. 54).

Furthermore, defects can exist in multiple charge states, especially if the species involved have higher valence (as an example, V_{Bi} has more possible charge states than V_{Ag}), giving rise to multiple transition levels (Box 2). For example, although the (+/0) transition of V_{Se} in Sb_2Se_3 is inactive (slow carrier capture), the (2 +/+) transition is fast, thus rendering V_{Se} a fast recombination centre[53]. Limitations of a single-trap model have been observed frequently, with the need to consider metastable charges or structural configurations that can also participate in the charge-trapping processes by introducing intermediate states[50,55,56].

Models for defect tolerance

Several models have been proposed in the literature to explain one or more aspects of the observed defect tolerance of metal halide perovskites.

High dielectric screening. The strength of the electrostatic interactions between charges in a crystal depends on the dielectric constant. This constant influences relevant processes, ranging from the binding energy between electrons and holes to form excitons, the scattering between charge carriers and charged defects that may limit mobility, and the rates at which defects capture and annihilate charge carriers. For example, a higher dielectric constant weakens the Coulomb attraction between charge carriers and charged defects, and thus reduces the carrier-capture coefficient (Fig. 2a). In standard inorganic semiconductors, the static dielectric constant is comprised of two components: a high-frequency optical response (ε_{optic}) and a low-frequency ionic response from phonons (ε_{ion}). For $CH_3NH_3PbI_3$, the reported values of ε_{optic} (4–7) are typical for photovoltaic absorbers, whereas those reported for ε_{ion} are substantially larger (17–29) due to the low-frequency infrared-active phonon modes and the unusually high Born effective charges, especially from Pb^{2+} (ref. 57). Unlike oxidation states, Born effective charges provide a dynamic measure of the atomic charges by capturing the effects from charge redistribution due to bonding and vibrations, with high Born effective charges leading to larger ε_{ion}. Finally, there is an additional component for the reorientation of the polar $CH_3NH_3^+$ molecule, which has been measured to have values between 13 and 37, depending on the temperature and frequency range. The combined contributions of the optical response, ionic response and molecular reorientation result in a dielectric screening that far exceeds the static dielectric constants of Si (12) or CdTe (10). These observations motivated the search for other highly polarizable semiconducting materials[30].

Box 2 | Predicting the role of point defects

Defect behaviour can be modelled at the atomic scale. The addition, removal or rearrangement of atoms in a crystal can be described using quantum mechanical methods (such as, density functional theory) or force fields (for example, classical or machine-learning interatomic potentials). The key thermodynamic quantity that influences many derived properties is the defect formation free energy ΔG_f, often approximated as defect formation enthalpy (ΔH_f)[237].

The advantage of quantum mechanical methods is that the electronic structure is rigorously described and there is no presumptive assumption on the type of bonding that occurs in the material or at the defect site. The main disadvantage is the high computational cost. Defect properties are also sensitive to choices in the level of theory, with a high level (that is, a hybrid exchange-correlation functional with relativistic effects) often required for accurate predictions of charge trapping with localized defect wavefunctions[26,37,58,238–240].

The first step of defect calculations consists of creating an atomic model for each native defect (for example, by removing a Bi^{3+} ion to model V_{Bi}^{3-} in Bi_2S_3). As defects can capture charge carriers from the host, thus undergoing structural rearrangements (see Box 1), a separate atomic model is needed for each charge state. Here, it is key that each atomic model represents the most stable defect geometry for each charge state to obtain accurate predictions[55,241–243]. The next step involves calculating the formation energy of each defect, which describes how easily they can form. These energies can be combined to predict the equilibrium concentrations and thus the dominant defect[244,245]. There is progress in automating many of these steps in software packages[246–251] such as 'doped'[252] and 'pydefect'[253].

The charge transition levels, which correspond to states that defects introduce within the bandgap, can also be analysed and are typically classified as resonant, shallow or deep. Generally, defects that introduce deep levels are considered to be potential recombination centres. However, the position of the defect levels is not a reliable proxy for recombination activity[37,54,254,255] (Box 1). Instead, the non-radiative recombination rate for each defect can be calculated using the capture coefficients for electrons and holes (modelling the process depicted in Box 1)[37,51,256,257] with packages like 'CarrierCapture'[258] and 'NonRad'[259]. By considering the recombination rates for all detrimental defects, the overall effect on photovoltaic efficiency can be predicted[234].

Equilibrium growth conditions are commonly assumed, which can be used as an avenue to tune the defect populations (for example through growth temperature, ratio of the precursor elements or partial pressure). By predicting defect concentrations for varying synthesis conditions, one can identify the conditions minimizing the density of harmful defects[6,35]. Another factor that can affect the concentration of efficiency-killing defects is the incorporation of extrinsic dopants. For instance, impurities can reduce the concentration of detrimental defects by passivating them[260] (for example by binding to the native defect to form a benign complex[28,261], like filling a vacancy site[53,262]). Alternatively, dopants can also act indirectly by modifying the density of free carriers (that is, the Fermi level), thus changing the concentration of the native defects[6] and their effect on non-radiative recombination[255,263].

Box 3 | Measuring the point defects present and their effects

The density, energy and capture cross-sections of defects, along with their effects on non-radiative recombination, can be determined using a wide range of spectroscopic, optical, electrical and capacitance techniques, as shown in the figure in this box. Owing to the multi-varied nature of how each technique works, we focus on the overarching principles, the strengths and the challenges of using each method on the materials considered in this Review.

Spectroscopic methods indirectly measure the effects of defects on non-radiative recombination, and they have the advantages of being non-destructive and not requiring pinhole-free films. Common techniques include steady-state photoluminescence quantum yield (measuring the fraction of recombination events that are radiative)[264] and time-resolved techniques, such as time-resolved photoluminescence[43,265] and transient absorption spectroscopy[266]. With these methods, the sample is optically pumped, but other pump sources can be used, such as electrons in cathodoluminescence spectroscopy[267] and positrons in positron annihilation lifetime spectroscopy[36]. Spectroscopic methods can also be applied to devices in which multiple excitation sources can be used to re-excite trapped carriers, producing changes in photocurrent that can be used to provide qualitative information on trap density[230,268,269]. Often these techniques are used together, but extracting recombination rate constants requires the development of a model to fit the time-resolved data[39,40], which is typically a simplification of the many complex processes occurring.

Relative changes in defect concentrations can be determined by measuring energetic transitions below the bandgap by tuning the energy of the probe beam of light (where *hv* is photon energy). However, the increase in sub-gap absorption due to defects is typically orders of magnitude below the band-edge absorption. Techniques sensitive to these small changes include photothermal deflection spectroscopy[270], surface photovoltage measurements[271] and Fourier transform photocurrent spectroscopy[272]. However, these techniques are unable to directly quantify defect densities or identify the defects present, and are more useful for qualitative comparisons between samples. In the figure, CBM stands for conduction band minimum and VBM for valence band maximum.

Quantification of defect concentrations can be achieved through space-charge-limited current density measurements[273]. This method requires a single-carrier device to be made, and the voltage (*V*) swept until traps are filled from the resulting electrical current (*I*). The trap density can be determined from the voltage at which trap-filling occurs, but this assumes an ideal device, which is often not the case. More accurate ways to quantify defect density, as well as capture cross-sections, involve monitoring changes in the capacitance (*C*) of a device due to trap filling or de-trapping. Prominent techniques include deep-level transient spectroscopy[274] and admittance spectroscopy[275], which are sensitive to defects at the parts per trillion level[276], but only deep-level transient spectroscopy can differentiate between electron and hole traps and measure their capture coefficients[277]. However, these techniques cannot directly identify the defects giving rise to the traps, they require the fabrication of devices (that is, they need compact films for analysis) and are unable to detect shallow defects[274,275]. Ion migration will affect the capacitance profiles, requiring consideration of how these affect the measurements[33]. Furthermore, deep-level transient spectroscopy and admittance spectroscopy may present lower estimates of trap densities, and such results need to be treated with caution.

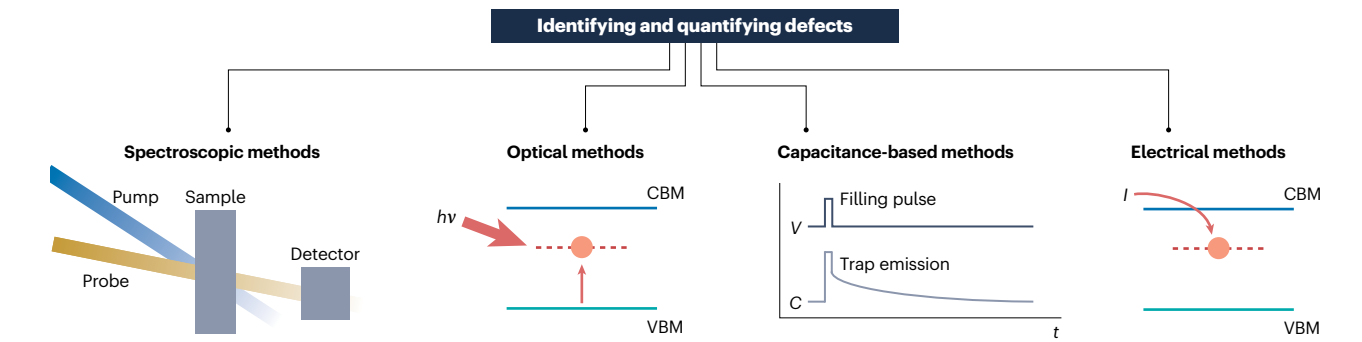

Shallow trap model. Most of the reported defect calculations for $CH_3NH_3PbI_3$ have concluded that the dominant intrinsic defects create mostly shallow levels[29,57,58] that result in low carrier-capture coefficients, thus partially explaining the long electron–hole diffusion lengths and high open-circuit voltage (V_{OC}). This observation does not mean that deep states cannot form; for example, there is a considerable body of literature on deep traps introduced by halide interstitials or lead antisites, but, fortunately, they do not support rapid non-radiative recombination cycles[59,60].

Microscopically, the tendency to form shallow traps was attributed to the anti-bonding nature of the upper valence band (Pb 6*s* − I 5*p*) and lower conduction band (Pb 6*p* − I 5*p*), as illustrated in Fig. 2b. In this orbital arrangement, the atomic orbitals from which non-bonding defect states arise are located close to the band edges, and thus often lead to shallow or resonant states[6,61]. However, deep states can still form when there is substantial hybridization between the defect dangling bonds, as the resulting (anti)bonding state will have (higher) lower energy than the original atomic orbitals[62]. Such behaviour is exemplified by the halide vacancy in the $CsPbX_3$ family, whose (+/0) donor level changes from shallow to deep through the halide series (I, Br, Cl)[52] due to the decreased lattice constant (thus smaller Pb–Pb distance in $CsPbCl_3$) and increased ionicity, which favour the hybridization of Pb

orbitals[63,64]. The relationship between increased lattice constants and reduced trap-mediated recombination has been further confirmed by the calculated carrier capture calculations of I_i in orthorhombic $FAPbI_3$, in which a 1% lattice expansion reduces the carrier capture coefficient by one order of magnitude[65].

Low density of deep defects. An argument put forward against the shallow defect model is that some low-energy defects (for example, V_H and I_i in $MAPbI_3$)[66,67] may act as rapid non-radiative recombination centres. However, these studies seem to be limited by either modelling less common defect species (that is, V_H corresponds to forming methylamine, CH_3NH_2, forming a gas that evaporates under typical synthesis and processing conditions) or disagreements with other theoretical studies that also investigated carrier capture by I_i[26,59,68]. More importantly, they would challenge the experimentally observed long charge-carrier lifetimes found in LHPs. These discrepancies between theoretical studies illustrate the challenges for accurately modelling defects in LHPs due to the instability of the cubic phase at 0 K and the soft potential energy surface that supports considerable thermal motion, including dynamic octahedral tilting around room temperature[68,69]. This soft potential energy surface and the chemical flexibility of the halide ions[26] have been linked to the observed low non-radiative recombination rates, as they result in large structural changes upon carrier capture that can increase the energetic barrier for one of the capture processes[59].

Self-compensation of defects. Most LHPs are intrinsic semiconductors, with low charge-carrier concentrations in the dark[70], and are resistant to extrinsic n-type or p-type doping. Sn-based compounds are an exception, due to the oxidation of Sn(II) to Sn(IV)[71]. One model used to explain the intrinsic behaviour, which can be beneficial to ensuring a low current in the dark and enhancing charge separation through a wide depletion region[72,73] in solar cells, is self-compensation. Rather than forming charged defects that are compensated by electrons or holes, the defects form in predominately charge-neutral combinations (Fig. 2d). Compensation can occur in the form of Schottky (vacancy) disorder, that is, $[V_A^-] + [V_B^{2-}] = 3[V_X^+]$, or Frenkel (vacancy/interstitial) disorder, that is, $[V_X^+] = [X_i^-]$[74]. The thermodynamic cost to form ensembles of compensated defects is low[74]. This introduces an insensitivity to the growth conditions, and large defect concentrations can be supported without the detrimental effects of high carrier concentrations that would otherwise reduce solar cell efficiency by limiting charge-carrier extraction. This model has been further validated by posterior theoretical studies on $MAPbI_3$, which predicted that the vacancies V_I^+, V_{Pb}^{2-} and V_{MA}^- form in high concentrations and follow a ratio ranging between 9.1:3.5:2 and 9.5:2.3:3.8 from MAI-rich to PbI_2-rich conditions, respectively. Therefore, they are in agreement with the formation of a stoichiometric amount of cation and anion vacancies[75]. In addition, the predicted high vacancy concentration supports the observed high ionic conductivities as they facilitate mass transport.

Polaronic model. Zhu and co-workers proposed that the defect tolerance of LHPs is linked to the formation of large polarons[76–78]. Large polarons arise due to the weak-to-intermediate coupling between charge carriers and longitudinal optical phonons, and there is now a plethora of evidence for large polaron formation from temperature-dependent mobility, optical pump terahertz probe spectroscopy, transient absorption spectroscopy and transient electron diffraction measurements, among others[46,76]. For example, calculations of the polaron radius for $CH_3NH_3PbBr_3$ and $CsPbBr_3$ perovskites give values an order of magnitude larger than the unit cell[79]. Zhu and co-workers speculated that the formation of large polarons could lead to reduced scattering by defects compared with free carriers, due to the higher effective mass and larger momentum. Additionally, the ionic distortions created by large polarons may add an extra energy barrier to the recombination of two large polarons with opposite charges, slowing down the recombination process and increasing the charge-carrier lifetime[76–78,80] (Fig. 2e). However, no detailed model has been put forward regarding this, and the balance between a reduction in electron–hole recombination due to dynamic shielding and the additional non-radiative channels that they open remains unexplored. Indeed, the recombination of electrons and holes via polarons could lower PLQY and reduce the overall photovoltaic performance of the material, even if the defect capture coefficient is reduced.

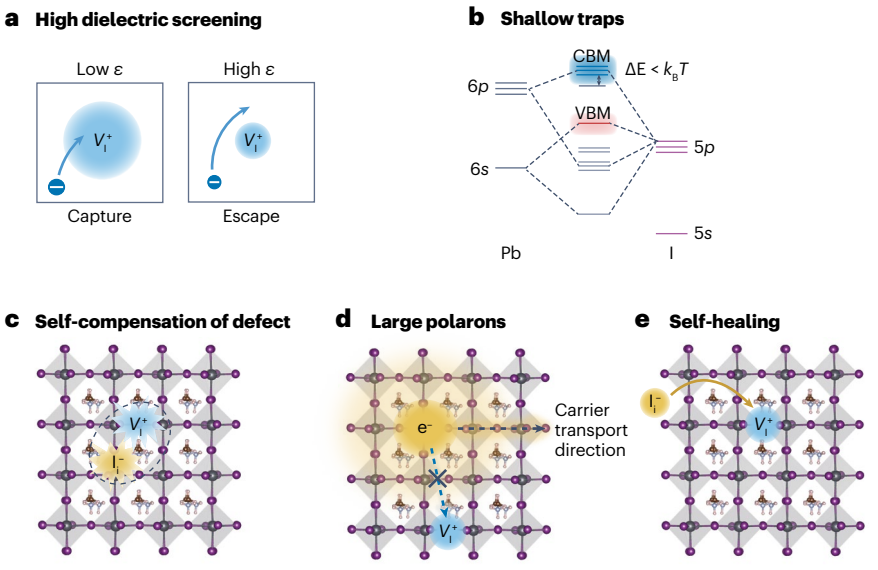

Fig. 2 | Models for defect tolerance in lead halide perovskites. a, High dielectric screening, in which the high dielectric constants reduce the strength of the interaction between free charge carriers and charged defects (V_I^+), thereby reducing the rate of carrier capture. **b**, Shallow trap model, in which most traps are close to band edges (within a few $k_BT - k_B$, Boltzmann's constant; T, temperature), and therefore benign. **c**, Self-compensation of defects, in which defects form in charge-neutral combinations (such as V_I^+ and I_i^-). **d**, Large polaron and low phonon energy model, in which large polarons reduce the scattering and capture of charge carriers by charged traps, and the low phonon energy leads to trapping being more difficult, with reduced nonadiabatic coupling constants. **e**, Self-healing, in which fast ion migration promotes the annihilation of defects formed during exposure to damaging conditions. CBM, conduction band minimum; e^-, electron; ε, dielectric constant; VBM, valence band maximum.

One disadvantage of large polarons is the reduction in charge-carrier mobility. Fortunately, the low deformation potential in electronically 3D halide perovskites ensures that small polarons do not form, such that charge carriers remain delocalized, and mobilities >50–200 $cm^2 V^{-1} s^{-1}$ are achievable[81]. Polycrystalline thin films can have lower mobilities on the order of 2 $cm^2 V^{-1} s^{-1}$ due to additional scattering processes, but this is still sufficient for achieving >1 µm diffusion lengths because of the long charge-carrier lifetimes[82].

Low-energy phonons. A key feature of LHPs is the soft nature of their structure comprised of flexible corner-sharing octahedra, with bulk moduli an order of magnitude smaller than metal oxides[83,84] (such as, 20 ± 2 GPa for $MAPbI_3$ (ref. 85) versus 390 GPa for α-Al_2O_3 (ref. 86)). The underlying vibrational spectrum is complex, ranging from low-frequency modes (<100 cm^{-1}), associated with octahedral tilting and deformations, to high-frequency modes (>100 cm^{-1}), linked to molecular vibrations[87]. The low-frequency infrared-active phonon modes make the largest contribution to electron–phonon coupling and result in an upper limit to the charge-carrier mobility[88]. Kirchartz et al. pointed out that within the Shockley–Read–Hall model of non-radiative recombination, a low phonon energy is beneficial. As carrier trapping is a multi-phonon emission process, a larger number of phonons need to be emitted if the phonon energy is smaller, making carrier trapping less likely to occur (that is, a lower capture coefficient)[89]. The role of phonon modes has also been explored using non-adiabatic molecular dynamics simulations that track the non-adiabatic coupling constant between electrons and holes with defect states at finite temperatures. Low non-adiabatic coupling constant values have been linked to defect tolerance, including contributions from differences in wavefunction overlap, as well as contributions from the nuclear velocity of the heavy Pb and I atoms[83,84]. Although non-adiabatic molecular dynamics is useful to model the dynamics of defects in excited states, it is important to consider all recombination mechanisms with appropriate charge-carrier and defect densities to estimate the contributions of changes in non-adiabatic coupling constant to device performance. These factors can increase the predicted carrier lifetimes from nanoseconds to miliseconds[90].

Dynamic local symmetry breaking. As well as being low-energy, the phonon modes of LHPs are highly anharmonic, as indicated by observables such as large thermal expansion coefficients, short phonon lifetimes and highly structured diffuse scattering. One consequence of phonon anharmonicity is that the local structure can deviate from the global average structure at short timescales. This can occur through BX_6 octahedral rotations and/or cation off-centring of the ions, which has been observed in chalcogenides and LHPs at temperatures above the cubic phase transition[91–93]. Breaking of the B-site centrosymmetry, described as a dynamic second-order Jahn–Teller distortion or emphanisis, results in a weak expression of the B-site ns^2 lone pair, which can re-orient itself in response to the orientation of other nearby lone pairs, or the presence of charged lattice species such as defects or polarons[92,94]. This can result in the formation of nanoferroelectric domains and enhanced dielectric screening of charged species, in which the latter can contribute to defect tolerance by spatially separating the charge carriers, and thus suppressing electron–hole recombination. Dynamic symmetry breaking is hidden in typical Bragg-like diffraction experiments (which only gives the average structure) but can be revealed by techniques probing the local structure and dynamics, such as pair distribution function analysis. The stability of the ns^2 lone pair may be tuned primarily by changing the chemical identity of B-site cation and halide anion[92,95], although the choice of the A-site cation has been shown to influence local ordering as well[94].

Self-healing. This refers to the ability of a material to autonomously recover its original performance after being damaged by an external stressor (Fig. 2f). It has been proposed to explain the high radiation resistance of LHPs[96–98] and their performance recovery during light–dark cycles[99–102]. Microscopically, self-healing has been attributed to rapid ion migration[24,79,96,99]. External perturbations, like high-energy radiation[96], light illumination[99], stress[103], crystal cleavage[104] or chemical agents, can create defects. After the perturbation ceases, ions can migrate and return to their energetically favoured lattice positions, thus annihilating the defects[105]. Beyond defect migration, self-healing has also been linked to the low dissociation energy of LHPs into their binary constituents[106], which enables the rapid reformation of the LHP after damage. For example, the self-healing behaviour induced by chemical agents was investigated by Zhou and co-workers, who demonstrated that a mild stimulus (methylamine gas) can induce the collapse of the perovskite structure into an intermediate liquid phase, which transforms into a smooth 'defect-free' film, once the gas is removed[107].

Challenges in generalizing defect tolerance

A core motivation for unravelling the origins of defect tolerance in LHPs is to replicate this feature in broader classes of semiconductors, particularly nontoxic and stable compounds. Semiconductors developed on this basis are termed 'perovskite-inspired' and have especially focused on materials with heavy main group cations that have stable valence ns^2 electron pairs (In^+, Sn^{2+}, Sb^{3+} and Bi^{3+}). In this section, we cover key points in the progress of these materials in photovoltaics, before discussing the challenges in obtaining defect tolerance in chemistries beyond halide perovskites.

Progress of perovskite-inspired materials in photovoltaics

To give a sense of the progress in this area, we cover key perovskite-inspired materials (PIMs), namely Sn and Ge perovskites, Bi-based compounds and antimony chalcogenides. These are most relevant for the discussion below, but a more detailed coverage of this broad materials space, including In-based compounds, can be found elsewhere[108–112]. Although the exploration of some compounds predates the development of LHP photovoltaics, it is useful to consider these as PIMs, because they are electronically, structurally or chemically analogous to LHPs, and the motivation is the same—to develop an efficient, nontoxic and stable alternative to halide perovskite photovoltaics.

Sn and Ge perovskites. The greatest successes have been in materials most similar to LHPs, the isostructural tin-based perovskites ($ASnI_3$, with the cation A∈{methylammonium (MA), formamidinium (FA), Cs})[113–135]. $FASnI_3$ photovoltaics have now reached PCEs of 15.7% (Fig. 3), with a photoluminescence lifetime of 207 ns. However, Sn perovskites have limited stability, due to the facile oxidation of Sn(II) to Sn(IV), forming reactive defects that accelerate degradation. As such, excess SnX_2 halides and reducing additives, such as Sn powder, hydrazine vapour, and hydrazine-derived compounds, are widely used in high-efficiency Sn perovskite solar cells[136]. Careful encapsulation of Sn perovskite devices, or the formation of protective layers (such as $SnCl_2$ covering grains) are essential[137]. Similarly, Ge(II) is easily oxidized,

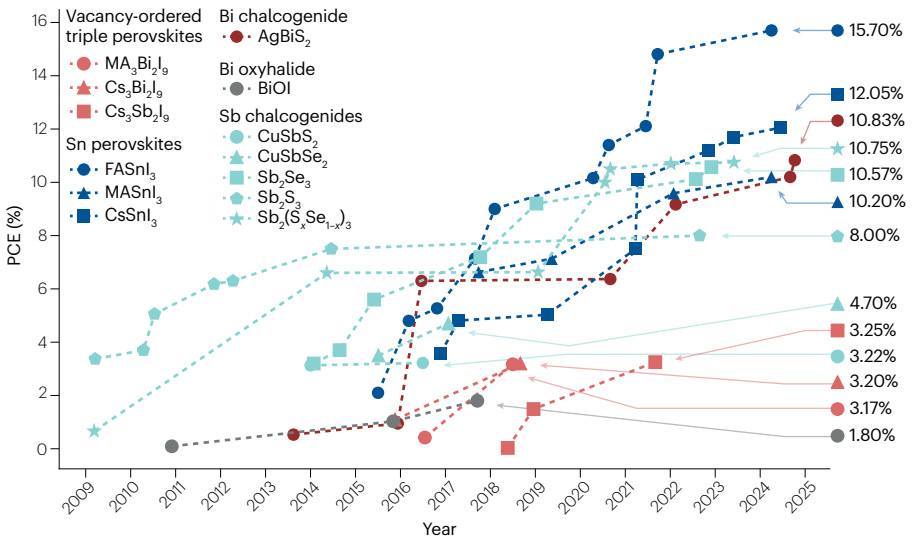

Fig. 3 | Progress of perovskite-inspired materials as solar absorbers. Plot of the progress in the photovoltaic power conversion efficiency (PCE) over time of key compounds. References by material: $MA_3Bi_2I_9$ (ref. 151), $Cs_3Bi_2I_9$ (refs. 142,143), $Cs_3Sb_2I_9$ (refs. 184–186), $FASnI_3$ (refs. 113–123), $MASnI_3$ (refs. 124–127), $CsSnI_3$ (refs. 128–135), $AgBiS_2$ (refs. 144–148,156), BiOI[149,150,192], $CuSbS_2$ (refs. 181,182), $CuSbSe_2$ (refs. 157,183), Sb_2S_3 (refs. 164–170), Sb_2Se_3 (refs. 158–163), $Sb_2(S_xSe_{1-x})_3$ (refs. 171–177). See Supplementary Information for details. FA, formamidinium; MA, methylammonium.

leading to the formation of detrimental defects and competitive phases[138,139], and, with few exceptions, most Ge-based perovskites (for example, $CsGeI_3$) have bandgaps exceeding 2 eV[140]. There is therefore limited work on Ge-based perovskites.

Bi-based materials. Although Bi-based compounds have been the subject of much research due to their low toxicity[141–150], a common characteristic of these materials is self-trapping, which substantially limits mobilities and diffusion lengths, gives rise to larger V_{OC} losses, and can lead to unavoidable energy loss channels (see Carrier–phonon coupling section for further discussion). As such, many Bi-based materials perform poorly, including $MA_3Bi_2I_9$ (ref. 151), $NaBiS_2$ (ref. 152) and BiI_3 (ref. 153), all of which form small polarons or self-trapped excitons. However, work has shown that self-trapping is not universal among Bi-based materials, and both BiOI and homogenously disordered $AgBiS_2$ have mobilities greatly above unity[154,155]. There is therefore hope that Bi-based PIMs could be developed into efficient devices, and indeed $AgBiS_2$ has already reached a certified PCE of 8.85%[156], with lab-measured PCEs now exceeding 10%[157] (Fig. 3).

Antimony chalcogenides. The isostructural antimony chalcogenides Sb_2Se_3 (refs. 158–163), Sb_2S_3 (refs. 164–170) and $Sb_2(S_xSe_{1-x})_3$ (refs. 171–177) are promising systems, with the highest reported efficiencies of 10.57%[178], 8.00%[164] and 10.75%[171], respectively, but they are limited by low V_{OC} values. Of the binary compounds, the selenide analogue shows the best efficiencies, in which process control of the defects present is key to high-efficiency devices. There has been some debate over whether the critical performance losses originate from deep defects or self-trapping (see Carrier–phonon coupling section). Nevertheless, reducing the grain boundary density and passivating interfaces (for example through the use of chelating or lanthanide additives) has been beneficial for improving V_{OC} and device performance[179,180].

Ternary cuprous compounds include $CuSbSe_2$ and $CuSbS_2$, both of which showed early promise in their performance[157,181], have since stagnated (with peak PCEs of 4.7%[182] for $CuSbSe_2$ and 3.2%[183] for $CuSbS_2$; Fig. 3 (refs. 184–186)). These isostructural materials were predicted to be defect-tolerant[187]. For both materials, a Cu-poor growth condition is preferred, as the dominant V_{Cu} results in p-type character via self-compensation. The poor performance has been attributed to low short-circuit current density values, yet the reasons remain unexplored[188]. Morphological defects, such as voids and delamination, are also common and device-limiting. Additionally, it has been proposed that grain boundary defects may be strongly detrimental in this class, as with CdTe[21,22].

Challenges in achieving defect tolerance in perovskite-inspired materials

The development of PIMs has provided an opportunity to evaluate the strengths, generalizability and limitations of the design principles for defect tolerance proposed for LHPs, which has in turn enabled refinements to be made.

Diversity of the electronic structure. Early efforts to discover PIMs were driven by dielectric screening and shallow trap models[30,39] (Fig. 2a,b). However, these models have not been able to pinpoint the discovery of defect-tolerant semiconductors. For example, Zakutayev et al. proposed an electronic structure model for defect tolerance in Cu_3N resembling the model for LHPs. In Cu_3N, cation–anion orbital interactions produce a pair of bonding–antibonding states in both the upper valence and lower conduction bands[31] (Fig. 4a). Although this was initially proposed to increase the likelihood of forming shallow defects[31], work has since suggested the copper interstitial Cu_i to be a potential deep trap[189]. LHPs similarly form a bonding–antibonding pair within the upper valence band, although the conduction band minimum has an antibonding state (Fig. 2b). Such an electronic structure increases the likelihood of shallow acceptor defects. Buonassisi and co-workers therefore proposed to search for PIMs in which the upper valence band has a considerable contribution from the cation valence s^2 electrons, as they could result in a qualitatively similar electronic structure at the band edges as LHPs[30,39].

However, this qualitative model does not account for the degree of interaction between cation and anion orbitals or the specific crystal environments. In particular, Bi has a higher effective nuclear charge than Pb, and this results in the $6s^2$ orbital being deeper and more

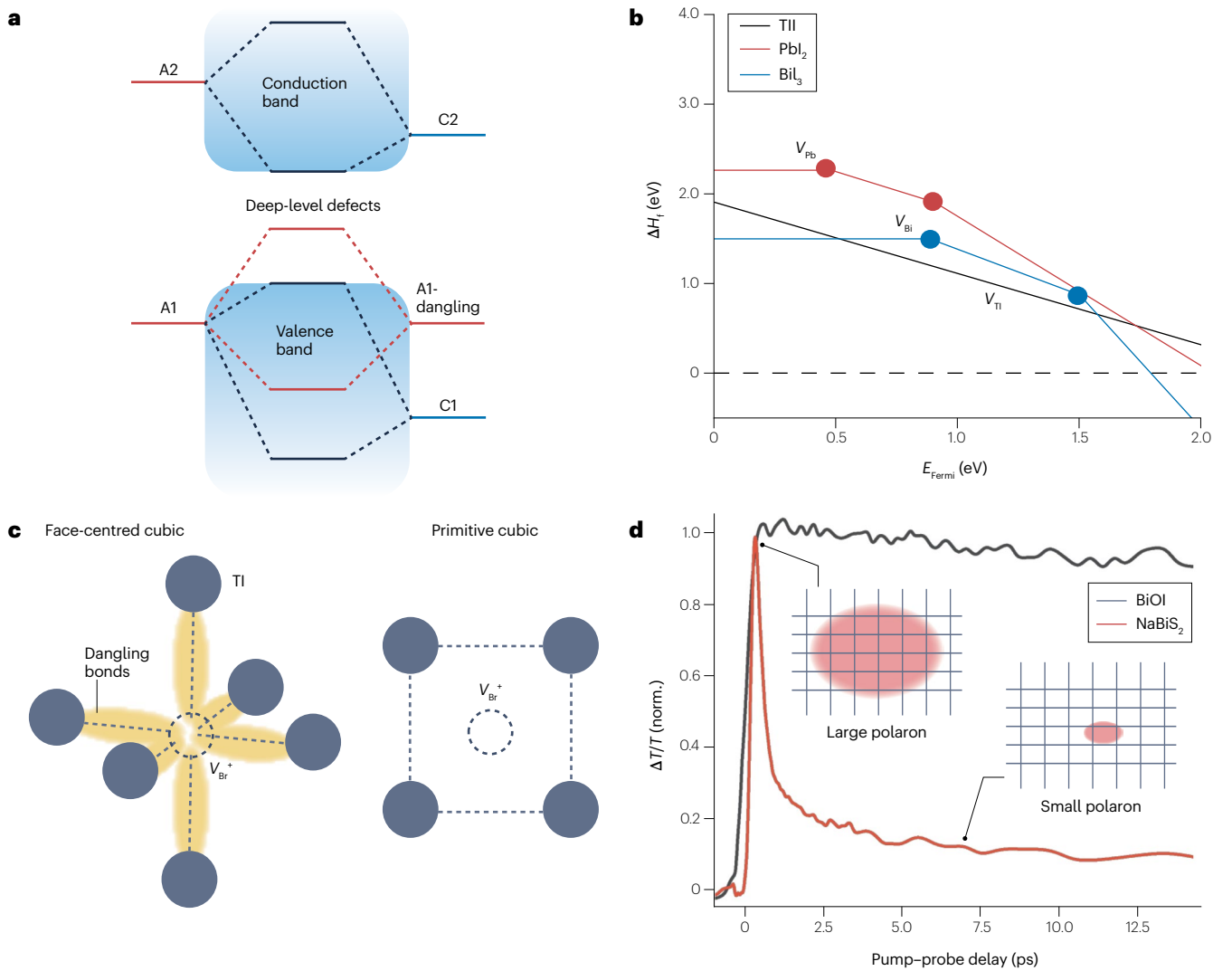

Fig. 4 | Performance bottlenecks in emerging perovskite-inspired materials. **a**, Energy misalignment leading to the presence of deep defects. A, A-dangling and C refer to the anion, anion dangling bond and cation orbitals, respectively[190]. **b**, Calculated formation energies ΔH_f of the cation vacancies in TlI, PbI_2 and BiI_3 (V_{Ti}, V_{Pb} and V_{Bi}, respectively) versus the energy of the Fermi level E_{Fermi}[190]. **c**, Strong overlap of dangling bonds due to V_{Br}^+ vacancy defect in a face-centred cubic lattice of TlBr (left) versus weak dangling bond overlap in the primitive cubic polymorph (right). **d**, Normalized (norm.) photoconductivity kinetics of BiOI and $NaBiS_2$ (refs. 152,155). In $NaBiS_2$, delocalized large polarons initially occur after photoexcitation, but due to strong electron–phonon coupling, small polarons rapidly form on a ps timescale, leading to localized small polarons and a sharp decrease in photoconductivity. By contrast, the photoconductivity of BiOI slowly decays because carrier localization does not occur.

misaligned with the anion orbitals, resulting in a less disperse valence band (higher effective mass), along with an increased tendency to form deeper traps.

Strength of interactions between dangling bonds. When defects form, dangling bonds can hybridize, forming bonding–antibonding states. The (anti)bonding states can occur within the bandgap, becoming recombination-active traps (Fig. 4a). Stronger hybridization leads to a greater bonding–antibonding state splitting, increasing the likelihood of deep traps. This hybridization strength between dangling bonds depends on their spatial and energetic separation. Therefore, traps become deeper when the lattice parameter decreases (see Shallow trap model sub-section) or when the cation–anion orbitals are more poorly aligned (that is, as C1 is further from A1 in Fig. 4a). For example, in comparing iodides of heavy main group cations with stable $6s^2$ electron pairs (Tl to Bi), the cation vacancy forms a deeper level going across this series (Fig. 4b) due to the increasing energetic separation between cation–anion orbitals (C1–A1 in Fig. 4a). Furthermore, the higher cation oxidation state leads to a larger number of transition levels (Fig. 4b), thus increasing the likelihood of deep traps[190]. The role of spatial separation can be illustrated by BiOI, in which the long Bi–I bonds (3.4 Å) weaken the interaction between Bi dangling orbitals, thus forming a shallow iodine vacancy V_I, in contrast with the deeper oxygen vacancy V_O and the shorter Bi–O bonds (2.3 Å)[191,192].

The strength of the interactions between dangling bonds is also affected by the ionic radius and anion coordination number. For instance, large anions coordinated with small cations, as well as low anion coordination numbers, have larger inter-cation separation, which could result in shallow anion vacancies[190].

The discussion thus far has been on compounds in which the cation and anion orbitals hybridize. Another way to form shallow traps involves materials with little interaction between the cation and anion orbitals, such that forming vacancies would not lead to dangling bonds. This could be obtained either by forming a structure with separate cation and anion sub-lattices (such as TlBr in the primitive cubic rather than face-centred cubic lattice; Fig. 4c)[193], or by having cation and anion orbitals with sufficient energetic separation to avoid mixing (such as in monolayer transition metal dichalcogenides)[194].

Low dimensionality. A critical difference between most of the PIMs explored and LHPs is the lower structural and electronic dimensionality of PIMs, leading to important challenges. First, excitons can form more easily, impeding charge-carrier extraction. Second, lower dimensionality favours wider bandgaps, with values close to 2 eV[195] for most PIMs versus 1.5–1.6 eV for $MAPbI_3$ (refs. 196,197). A wider bandgap reduces the optical dielectric constant, as fewer free carriers are available for polarization, thus reducing the dielectric screening of charged defects. Third, in some cases, low dimensionality could facilitate defect formation. For example, although Sb_2Se_3 has been considered promising because it has achieved >10% PCE in photovoltaic devices (Fig. 3), both density functional theory calculations and DLTS measurements indicate its lack of defect tolerance[53,198,199]. This has been attributed to the quasi-1D crystal structure of Sb_2Se_3, in which the $[Sb_4Se_6]_n$ chains are bonded through van der Waals interactions. These weak interactions, in addition to the valence alternation of Sb and Se[200], allow substantial structural reconstructions upon defect formation, thus stabilizing many charge states and leading to many defect levels. Finally, low electronic dimensionality also increases the likelihood of carrier localization, as is discussed next.

Carrier–phonon coupling. Charge carriers can couple with lattice vibrations, giving rise to quasi-particles known as polarons[201]. Strong electron–phonon coupling can localize the carrier wavefunction within a unit cell, which is known as carrier localization or self-trapping. This substantially reduces mobilities (typically to <1–10 $cm^2 V^{-1} s^{-1}$), limiting diffusion lengths, and is unavoidable even in defect-free materials. Carrier localization can result in short diffusion lengths despite long charge-carrier lifetimes[156]. The past decade of work has revealed the considerable presence of self-trapping in PIMs, especially Bi-based materials[45,202,203], including BiI_3 (ref. 204), $NaBiS_2$ (ref. 152), Cu-Ag-Bi-I compounds[153,205], $Cs_2AgBiBr_6$ (ref. 202) and other silver-bismuth elpasolites. This originates from their low electronic dimensionality, which can lead to barrierless carrier localization, especially when there is strong carrier–acoustic phonon coupling. Such a process can be observed experimentally by monitoring the photoconductivity, in which the signal decreases markedly within a picosecond, as demonstrated in the case of $NaBiS_2$ (Fig. 4d).

Carrier localization can change the optoelectronic behaviour of materials, such that deep trap states no longer play a dominant role. For example, introducing defects at the percentage level in $NaBiS_2$ barely changed the decay of the excited state, which proceeded on the microsecond timescale[152]. This is due to the formation of small electron and hole polarons, spatially separated on Bi-rich and Na-rich regions, respectively, which lowers the likelihood of both charge carriers annihilating via the same defect. Although this gives the appearance of defect tolerance, strong localization leads to low charge-carrier mobilities (<0.1 $cm^2 V^{-1} s^{-1}$; Fig. 4d), thus limiting diffusion lengths and charge-carrier extraction. Developing efficient PIMs therefore necessitates compounds with free charge carriers. By studying $CuSbSe_2$, we rationalized that this may be found in compounds with a layered structure. This results in a lower deformation potential, because the strains to the unit cell from a propagating acoustic wave are mostly relaxed through changes in inter-layer gaps, rather than bond lengths or angles[206]. Furthermore, orbital hybridization across inter-layer gaps results in a higher electronic dimensionality[207]. For example, although $CuSbSe_2$ is structurally 2D, its lower conduction band has nearly 3D electronic dimensionality due to quasi-bonding across the inter-layer gaps. This higher electronic dimensionality reduces the likelihood of carrier localization being energetically favourable[206].

Finally, electron–phonon coupling can also create a non-radiative loss channel that does not arise from defects. This is found in BiOI, in which the coupling between charge carriers and interlayer breathing modes greatly distorts the potential energy surface, such that the ground and excited states approach each other, and excitations can then directly return to the ground state following a non-radiative pathway[208].

Improved methods to quantify defects

Experimentally probing defect tolerance is made challenging by the difficulties in accurately quantifying the concentration and energy of specific defects giving rise to the measured recombination coefficients[49,209–211]. This challenge is amplified in halide perovskite semiconductors because of the mixed ionic–electronic nature of charge transport[212,213], which is also a complication found in many PIMs[208,214]. Here, we discuss the advances made with emerging spectroscopy and microscopy techniques to address this limitation.

Spectroscopic techniques

Two of the most powerful techniques for quantifying the concentration and properties of defects are DLTS and PALS.

Deep-level transient spectroscopy. As discussed in Box 3, DLTS monitors the change in capacitance from carrier capture and emission from defects – and in conventional analysis, it is assumed that these defects are immobile. These traps are filled through a voltage or current pulse, but this can also cause ions to migrate, which also affects the capacitance signal[33,212,215]. Futscher and Deibel pointed out that both ionic and electronic defects can be probed by DLTS and are identified by comparing the time constants for the rise (τ_1) and fall (τ_2) in capacitance with the application of a voltage pulse (Fig. 5a). If electronic defects are probed, then $\tau_1 \ll \tau_2$. This is because τ_1 would be due to carrier capture whereas τ_2 would be due to carrier emission, and $\tau_1/\tau_2 = \exp(-E_T/k_BT)$, in which E_T is the trap energy, k_B is the Boltzmann's constant and T is the temperature[33]. τ_1/τ_2 can only be close to unity for shallow traps, but these cannot be resolved by DLTS, and so $\tau_1 \ll \tau_2$. By contrast, for ionic transport, τ_1 would be due to ion diffusion whereas τ_2 would be due to ionic drift, such that $\tau_1 \geq \tau_2$, as $\tau_1/\tau_2 = V/k_BT$, in which V in this equation is voltage. The timescales of capacitance rise and fall would also be longer, as ion migration takes place on the ms–s timescale, whereas carrier capture typically takes place over 10^{-13}–10^{-10} s[33]. The effects of ion migration could therefore be reduced by performing DLTS measurements at higher frequencies. However, if the activation

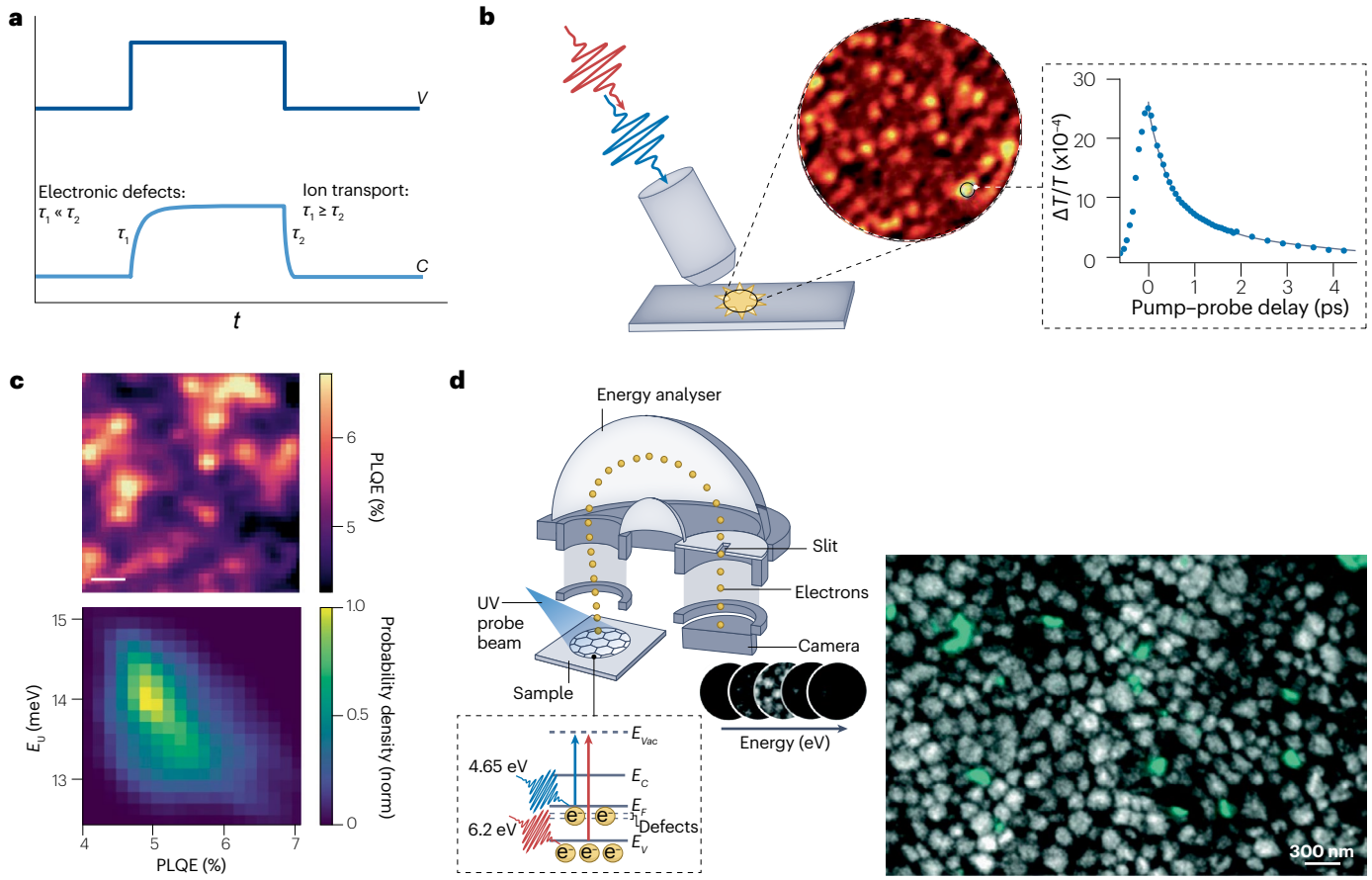

Fig. 5 | Emerging techniques to characterize point defects. a, Illustration of how the rise and fall of the capacitance (*C*) signal (with time constants τ_1 and τ_2, respectively) in deep-level transient spectroscopy measurements of mixed-ionic electronic conductors changes depending on whether measurements are dominated by electronic or ionic transport[33]. **b**, Diagram of transient absorption microscopy. **c**, Hyperspectral microscopy of lead halide perovskite film to obtain the photoluminescence quantum efficiency (PLQE) map (top: scale bar 1 µm) and Urbach energy (E_U) map over the same area, and the two properties correlated together (bottom). **d**, Schematic of photoemission electron microscopy (left) and example of the application of photoemission electron microscopy to image the morphology of a lead halide perovskite film (by mapping a valence band spectrum) with the map of trap states imaged from the same area superimposed on top. *t*, time; e^-, electron; norm., normalized; UV, ultraviolet; *V*, voltage; E_{Vac}, vacuum energy level; E_C, conduction band minimum; E_F, Fermi level; E_V, valence band maximum. Part **b** reprinted with permission from ref. 217, AIP. Part **c** reprinted from ref. 223, Springer Nature Limited. Part **d** is reprinted from ref. 227, under a Creative Commons licence CC BY 3.0.

energy barrier to ion migration is low, ionic defects will still dominate measurements, even at high frequencies[215]. Materials with suppressed ion migration, such as $(PEA)_2PbBr_4$ ($PEA^+ = C_6H_5C_2H_4NH_3^+$) or Sb_2Se_3, are necessary to observe electronic defects that are not obscured by ion migration[199,216].

Positron annihilation lifetime spectroscopy. This technique is advantageous with respect to DLTS in that it is not affected by ion migration because it probes the local environment of the defect that localizes the positron[36]. However, PALS is not able to directly identify the defects, requiring a comparison between the lifetime of positron states measured with calculated values for a model configuration to establish the nature of the defect. Furthermore, positrons localize in open-volume defects that are neutral or negative relative to the average structure. Therefore, PALS is better-suited to identifying neutral or negatively charged vacancies, and it may be insensitive to positively charged vacancies or other types of defects. For example, PALS can be used to identify negatively charged cation vacancies, but not the more abundant halide vacancies[36]. Using PALS, Keeble et al. identified Pb vacancies in $MAPbI_3$, with an estimated concentration of ~10^{17} cm^{-3}, to be present, and confirmed that methylammonium vacancies were absent, but they could not establish whether iodide vacancies, antisites or interstitials were present[36].

Microscopy techniques

The challenge with using microscopy techniques is improving the spatial resolution to understand defects with smaller length scales. Recent advances have also focused on bringing together spectroscopy with microscopy, enabling the effect of defects on variations in lifetime and luminescence on the micro-to-nanoscale to be resolved. This section discusses the advances and applications of transient absorption and photoluminescence microscopy, as well as photoelectron emission microscopy.

Transient absorption and photoluminescence microscopy. These are powerful techniques that can probe the spatial distribution of defects in a contactless and non-destructive manner under ambient conditions by combining time-resolved spectroscopy with microscopy (see Fig. 5b for transient absorption microscopy (TAM); photoluminescence microscopy has a similar setup[217]). TAM accounts for the total carrier population and is especially useful for understanding the role of defects in PIMs that have weak luminescence, for which photoluminescence mapping could not be used. TAM can be used to estimate defect concentrations from the pump fluence that saturates defect states[218,219], and it has been shown to be capable of resolving sub-gap defect signals obscured by noise in conventional transient absorption spectroscopy. This is because TAM can be focused to regions with high defect density, which represents an advantage over transient absorption spectroscopy[220]. In addition, by probing the broadening of TAM signals, the diffusion coefficients — and hence diffusion lengths in different regions — can also be estimated[221,222]. Although photoluminescence microscopy is not suitable for materials with weak luminescence, by only mapping carriers undergoing radiative recombination, photoluminescence microscopy provides larger signal contrast between regions of differing defect density[9,223–225] (Fig. 5c). The defects can be more directly probed by mapping PLQY based on photoluminescence microscopy[225]. This can be used to extract quasi-Fermi-level-splitting energy, which correlates to the V_{OC} loss for solar cells[43]. However, a limitation of most TAM and photoluminescence microscopy setups is that they only resolve down to ~100 nm and therefore can barely be used to image at the sub-grain level, let alone the point-defect level. Moreover, these techniques cannot be used to directly identify the defects imaged. They can, however, be correlated with compositional measurements over the same area (for example, from nano-X-ray fluorescence or transmission electron microscopy–energy -dispersive X-ray[223]. Correlative microscopy (Fig. 5c) is an important area to push forward regarding the understanding of how the processing of the materials affects the arrangement and nature of defects and how this (in turn) affects optoelectronic performance[226].

Photoemission electron microscopy. Finer spatial resolution can be obtained with photoemission electron microscopy (PEEM), which combines photoemission spectroscopy with microscopy by focusing the spot size of the incident ultraviolet (UV) beam used to generate photoelectrons, as well as magnifying the photoelectrons emitted with an electromagnetic lens (Fig. 5d). Spatial resolution on the order of tens of nanometres is achievable[227–229], which is still inadequate for imaging point defects but is useful for imaging trap clusters. These trap clusters manifest in the photoemission spectra as a photoelectron signal above the valence band maximum due to the emission of electrons from these trap states. By lowering the UV excitation energy to 4.65 eV, it was possible to only photoexcite electrons from these trap states without perturbing the valence band in mixed iodide–bromide perovskite films, enabling the mapping of trap clusters. These could be directly correlated with the microstructure of the material by mapping over the same area with a higher UV energy of 6.2 eV to emit photoelectrons from the valence band, providing grain boundary contrast[228] (Fig. 5d). Furthermore, time-resolved PEEM could be performed by photoexciting at an energy resonant with the bandgap of the material, followed by imaging the trap clusters with a time-delayed UV probe. The time resolution can be 300 fs (ref. 228), and modelling the decay in PEEM intensity from trap clusters allows the timescales for photogenerated holes to be captured by the trap clusters, and hence the size of the region affected. However, PEEM is unable to directly identify the nature of the clusters or how they affect the charge-carrier lifetime of the material. These goals can be achieved through correlative microscopy, in which the same region (with the help of fiducial markers) is imaged by PEEM, nano-X-ray diffraction (structure), nano-X-ray fluorescence (composition), transmission electron microscopy (composition and structure) and photoluminescence mapping. Such correlative measurements have revealed the important role of trap clusters at grain boundaries in triple-cation perovskite films in degrading performances, and how these could be mitigated through oxygen passivation[228]. PEEM can therefore provide powerful information and broaden the discussion of defect tolerance towards larger length scales than point defects.

Conclusions and outlook

Defect tolerance is key to developing high-performance and cost-effective optoelectronic materials. The exceptional performance of LHPs has revived this topic, which has been examined from a wide range of perspectives. Although this has led to different interpretations, at its core, we define defect tolerance to mean that the semiconductor maintains free charge carriers, low non-radiative recombination rates and high mobilities, despite the introduction of defects, which then affords it with the long charge-carrier transport lengths necessary to approach its optical limits in performance. A wide range of models have been proposed for defect tolerance in LHPs. The most popular are the shallow trapping and dielectric screening models, but they have yielded only few materials that may exhibit defect tolerance, and none that have yet matched the performance of LHP photovoltaics. A key issue is that these models do not account for the strength of cation–anion orbital overlap, or the hybridization between dangling bonds. Detailed studies into binary halide PIMs have proven valuable in refining these design criteria. At the same time, there are still several outstanding questions that need to be addressed.

First, the soft and dynamic nature of the LHP structure has complicated the interpretation of the role of traps via the Shockley–Read–Hall model, questioning whether the trap energy is a reasonable proxy for the carrier capture rate. In-depth investigations combining high-level theory with state-of-the-art characterization that can probe similar length-scales and time-scales will be necessary to quantify the fluctuations in charge transition levels and resolve this debate.

Second, a greater mechanistic understanding of self-healing is required, which will establish the importance of ion transport both in the dark and under illumination. Self-healing is poorly understood computationally due to the long timescales involved, but there is growing experimental evidence of its importance for the manifestation of defect tolerance in LHPs. If self-healing requires considerable mass transport, this would open up important questions regarding whether there would be a compromise with the stability of devices under operation.

Third, it will be critical to consider the role of carrier–phonon coupling. Although carrier localization may be considered distinct to defect tolerance, from the discussion in this Review, it can be seen that this effect plays a critical role in PIMs, and it should be studied alongside defect tolerance. This includes understanding whether a trade-off is required between factors affecting both of these effects. For example, lower-energy phonon modes contribute to defect tolerance but would increase the strength of electron–phonon coupling, reducing mobilities. Similarly, higher Born effective charges increase the ionic contribution to the dielectric constant, which leads to improved screening of carriers from charged defects, but would

also increase the strength of electron–phonon coupling. Beyond the current focus on band-edge charge carriers, an important challenge will be to extend the understanding of defect tolerance to hot carriers. In particular, understanding how traps influence the hot carrier cooling process, hot phonon bottleneck effect, Auger reheating and the overlap of polarons will be critical to achieving hot carrier solar cells that can exceed the Shockley–Queisser limit of a single-junction solar cell[230], with a theoretical efficiency limit >50%[231,232].

Finally, research efforts on defect tolerance have focused on linking the chemistry of materials with non-radiative recombination[68]. Mobility is also a critical parameter, and future efforts should investigate the effect of defects on charge-carrier transport, for example through impurity scattering or carrier capture (requiring hopping transport).

Overall, addressing these challenges could improve our understanding of the multifaceted nature of defect tolerance, not only for the current focus on intrinsic defects but also extended to extrinsic impurities[233]. Fully understanding the tolerance of materials to more complex defect systems requires the continued refinement of correlative, multimodal characterization tools. This technique development, in concert with an improved conceptual understanding of defect tolerance, can lead to new avenues to create efficient and cost-effective semiconductors.

Published online: 7 April 2025

References

1. Ballif, C., Haug, F.-J., Boccard, M., Verlinden, P. J. & Hahn, G. Status and perspectives of crystalline silicon photovoltaics in research and industry. *Nat. Rev. Mater.* **7**, 597–616 (2022).
2. Nayak, P. K., Mahesh, S., Snaith, H. J. & Cahen, D. Photovoltaic solar cell technologies: analysing the state of the art. *Nat. Rev. Mater.* **4**, 269–285 (2019).
3. Nishiyama, H. et al. Photocatalytic solar hydrogen production from water on a 100-m^2 scale. *Nature* **598**, 304–307 (2021).
4. Andrei, V. et al. Floating perovskite-$BiVO_4$ devices for scalable solar fuel production. *Nature* **608**, 518–522 (2022).
5. Holmes-Gentle, I., Tembhurne, S., Suter, C. & Haussener, S. Kilowatt-scale solar hydrogen production system using a concentrated integrated photoelectrochemical device. *Nat. Energy* **8**, 586–596 (2023).
6. Walsh, A. & Zunger, A. Instilling defect tolerance in new compounds. *Nat. Mater.* **16**, 964–967 (2017).
7. Zhou, Y., Poli, I., Meggiolaro, D., De Angelis, F. & Petrozza, A. Defect activity in metal halide perovskites with wide and narrow bandgap. *Nat. Rev. Mater.* **6**, 986–1002 (2021).
8. Zhou, J. et al. Highly efficient and stable perovskite solar cells via a multifunctional hole transporting material. *Joule* **8**, 1691–1706 (2024).
9. Liu, S. et al. Buried interface molecular hybrid for inverted perovskite solar cells. *Nature* **632**, 536–542 (2024).
10. Dale, P. J. & Scarpulla, M. A. Efficiency versus effort: a better way to compare best photovoltaic research cell efficiencies? *Sol. Energy Mater. Sol. Cells* **251**, 112097 (2023).
11. Tiedje, T., Yablonovitch, E., Cody, G. D. & Brooks, B. G. Limiting efficiency of silicon solar cells. *IEEE Trans. Electron. Devices* **31**, 711–716 (1984).
12. Akkerman, Q. A., Rainò, G., Kovalenko, M. V. & Manna, L. Genesis, challenges and opportunities for colloidal lead halide perovskite nanocrystals. *Nat. Mater.* **17**, 394–405 (2018).
13. Huang, H., Bodnarchuk, M. I., Kershaw, S. V., Kovalenko, M. V. & Rogach, A. L. Lead halide perovskite nanocrystals in the research spotlight: stability and defect tolerance. *ACS Energy Lett.* **2**, 2071–2083 (2017).
14. Xu, J. et al. Defect tolerance of mixed B-site organic–inorganic halide perovskites. *ACS Energy Lett.* **6**, 4220–4227 (2021).
15. Ye, J. et al. Defect passivation in lead-halide perovskite nanocrystals and thin films: toward efficient LEDs and solar cells. *Angew. Chem. Int. Ed.* **60**, 21636–21660 (2021).
16. Shin, S. S. et al. Colloidally prepared La-doped $BaSnO_3$ electrodes for efficient, photostable perovskite solar cells. *Science* **356**, 167–171 (2017).
17. Polman, A., Knight, M., Garnett, E. C., Ehrler, B. & Sinke, W. C. Photovoltaic materials: present efficiencies and future challenges. *Science* **352**, aad4424 (2016).
18. Lindmayer, J. & Allison, J. F. The violet cell: an improved silicon solar cell. *Sol. Cells* **29**, 151–166 (1990).
19. Green, M. A. The path to 25% silicon solar cell efficiency: history of silicon cell evolution. *Prog. Photovolt.* **17**, 183–189 (2009).
20. Green, M. A. Silicon solar cells: evolution, high-efficiency design and efficiency enhancements. *Semicond. Sci. Technol.* **8**, 1 (1993).
21. Blakesley, J. C. et al. Roadmap on established and emerging photovoltaics for sustainable energy conversion. *J. Phys. Energy* **6**, 041501 (2024).
22. Das, S. K. & Morris, G. C. Preparation and properties of CdS/CdTe thin film solar cell produced by periodic pulse electrodeposition technique. *Sol. Energy Mater. Sol. Cells* **30**, 107–118 (1993).
23. Park, J. et al. Controlled growth of perovskite layers with volatile alkylammonium chlorides. *Nature* **616**, 724–730 (2023).
24. Cahen, D., Kronik, L. & Hodes, G. Are defects in lead-halide perovskites healed, tolerated, or both? *ACS Energy Lett.* **6**, 4108–4114 (2021).
25. Min, H. et al. Efficient, stable solar cells by using inherent bandgap of α-phase formamidinium lead iodide. *Science* **366**, 749–753 (2019).
26. Meggiolaro, D. et al. Iodine chemistry determines the defect tolerance of lead-halide perovskites. *Energy Environ. Sci.* **11**, 702–713 (2018).
27. Hangleiter, A. Nonradiative recombination via deep impurity levels in silicon: experiment. *Phys. Rev. B* **35**, 9149–9161 (1987).
28. Zhang, S. B., Wei, S.-H. & Zunger, A. Stabilization of ternary compounds via ordered arrays of defect pairs. *Phys. Rev. Lett.* **78**, 4059–4062 (1997).
29. Yin, W.-J., Shi, T. & Yan, Y. Unusual defect physics in $CH_3NH_3PbI_3$ perovskite solar cell absorber. *Appl. Phys. Lett.* **104**, 063903 (2014).
30. Brandt, R. E., Stevanović, V., Ginley, D. S. & Buonassisi, T. Identifying defect-tolerant semiconductors with high minority-carrier lifetimes: beyond hybrid lead halide perovskites. *MRS Commun.* **5**, 265–275 (2015).
31. Zakutayev, A. et al. Defect tolerant semiconductors for solar energy conversion. *J. Phys. Chem. Lett.* **5**, 1117–1125 (2014).
32. Cohen, A., Egger, D. A., Rappe, A. M. & Kronik, L. Breakdown of the static picture of defect energetics in halide perovskites: the case of the Br vacancy in $CsPbBr_3$. *J. Phys. Chem. Lett.* **10**, 4490–4498 (2019).
33. Futscher, M. H. & Deibel, C. Defect spectroscopy in halide perovskites is dominated by ionic rather than electronic defects. *ACS Energy Lett.* **7**, 140–144 (2022).
34. Heo, S. et al. Deep level trapped defect analysis in $CH_3NH_3PbI_3$ perovskite solar cells by deep level transient spectroscopy. *Energy Environ. Sci.* **10**, 1128–1133 (2017).
35. Yang, W. S. et al. Iodide management in formamidinium-lead-halide–based perovskite layers for efficient solar cells. *Science* **356**, 1376–1379 (2017).
36. Keeble, D. J. et al. Identification of lead vacancy defects in lead halide perovskites. *Nat. Commun.* **12**, 5566 (2021).
37. Zhang, X., Turiansky, M. E., Shen, J.-X. & Van de Walle, C. G. Defect tolerance in halide perovskites: a first-principles perspective. *J. Appl. Phys.* **131**, 090901 (2022).
38. Jaramillo, R. et al. Transient terahertz photoconductivity measurements of minority-carrier lifetime in tin sulfide thin films: advanced metrology for an early stage photovoltaic material. *J. Appl. Phys.* **119**, 035101 (2016).
39. Brandt, R. E. et al. Searching for "defect-tolerant" photovoltaic materials: combined theoretical and experimental screening. *Chem. Mater.* **29**, 4667–4674 (2017).
40. Richter, J. M. et al. Enhancing photoluminescence yields in lead halide perovskites by photon recycling and light out-coupling. *Nat. Commun.* **7**, 13941 (2016).
41. Yuan, Y., Yan, G., Dreessen, C. & Kirchartz, T. Understanding power-law photoluminescence decays and bimolecular recombination in lead-halide perovskites. *Adv. Energy Mater.* **15**, 2403279 (2024).
42. Yuan, Y. et al. Shallow defects and variable photoluminescence decay times up to 280 μs in triple-cation perovskites. *Nat. Mater.* **23**, 391–397 (2024).
43. Kirchartz, T., Márquez, J. A., Stolterfoht, M. & Unold, T. Photoluminescence-based characterization of halide perovskites for photovoltaics. *Adv. Energy Mater.* **10**, 1904134 (2020).
44. Rondiya, S. R., Jagt, R. A., MacManus-Driscoll, J. L., Walsh, A. & Hoye, R. L. Z. Self-trapping in bismuth-based semiconductors: opportunities and challenges from optoelectronic devices to quantum technologies. *Appl. Phys. Lett.* **119**, 220501 (2021).
45. Wu, B. et al. Strong self-trapping by deformation potential limits photovoltaic performance in bismuth double perovskite. *Sci. Adv.* **7**, eabd3160 (2021).
46. Buizza, L. R. V. & Herz, L. M. Polarons and charge localization in metal-halide semiconductors for photovoltaic and light-emitting devices. *Adv. Mater.* **33**, 2007057 (2021).
47. Rau, U., Blank, B., Müller, T. C. M. & Kirchartz, T. Efficiency potential of photovoltaic materials and devices unveiled by detailed-balance analysis. *Phys. Rev. Appl.* **7**, 044016 (2017).
48. Green, M. A. & Ho-Baillie, A. W. Y. Pushing to the limit: radiative efficiencies of recent mainstream and emerging solar cells. *ACS Energy Lett.* **4**, 1639–1644 (2019).
49. Jasti, N. P. et al. Experimental evidence for defect tolerance in Pb-halide perovskites. *Proc. Natl Acad. Sci. USA* **121**, e2316867121 (2024).
50. Kavanagh, S. R., Scanlon, D. O., Walsh, A. & Freysoldt, C. Impact of metastable defect structures on carrier recombination in solar cells. *Faraday Discuss.* **239**, 339–356 (2022).
51. Alkauskas, A., Yan, Q. & Van de Walle, C. G. First-principles theory of nonradiative carrier capture via multiphonon emission. *Phys. Rev. B* **90**, 075202 (2014).
52. Nenon, D. P. et al. Design principles for trap-free $CsPbX_3$ nanocrystals: enumerating and eliminating surface halide vacancies with softer Lewis bases. *J. Am. Chem. Soc.* **140**, 17760–17772 (2018).
53. Wang, X., Kavanagh, S. R., Scanlon, D. O. & Walsh, A. Upper efficiency limit of Sb_2Se_3 solar cells. *Joule* **8**, 2105–2122 (2024).
54. Kim, S., Park, J.-S. & Walsh, A. Identification of killer defects in kesterite thin-film solar cells. *ACS Energy Lett.* **3**, 496–500 (2018).
55. Kavanagh, S. R., Walsh, A. & Scanlon, D. O. Rapid recombination by cadmium vacancies in CdTe. *ACS Energy Lett.* **6**, 1392–1398 (2021).

56. Yang, J.-H., Shi, L., Wang, L.-W. & Wei, S.-H. Non-radiative carrier recombination enhanced by two-level process: a first-principles study. *Sci. Rep.* **6**, 21712 (2016).
57. Du, M. H. Efficient carrier transport in halide perovskites: theoretical perspectives. *J. Mater. Chem. A* **2**, 9091–9098 (2014).
58. Du, M.-H. Density functional calculations of native defects in $CH_3NH_3PbI_3$: effects of spin–orbit coupling and self-interaction error. *J. Phys. Chem. Lett.* **6**, 1461–1466 (2015).
59. Whalley, L. D. et al. Giant Huang–Rhys factor for electron capture by the iodine intersitial in perovskite solar cells. *J. Am. Chem. Soc.* **143**, 9123–9128 (2021).
60. Zhang, J., Zhang, X., Turiansky, M. E. & Van de Walle, C. G. Iodine vacancies do not cause nonradiative recombination in halide perovskites. *PRX Energy* **2**, 013008 (2023).
61. Zhang, S. B., Wei, S.-H., Zunger, A. & Katayama-Yoshida, H. Defect physics of the $CuInSe_2$ chalcopyrite semiconductor. *Phys. Rev. B* **57**, 9642–9656 (1998).
62. Huang, Y.-T., Kavanagh, S. R., Scanlon, D. O., Walsh, A. & Hoye, R. L. Z. Perovskite-inspired materials for photovoltaics and beyond—from design to devices. *Nanotechnology* **32**, 132004 (2021).
63. Kim, J., Chung, C.-H. & Hong, K.-H. Understanding of the formation of shallow level defects from the intrinsic defects of lead tri-halide perovskites. *Phys. Chem. Chem. Phys.* **18**, 27143–27147 (2016).
64. Ganose, A. M., Scanlon, D. O., Walsh, A. & Hoye, R. L. Z. The defect challenge of wide-bandgap semiconductors for photovoltaics and beyond. *Nat. Commun.* **13**, 4715 (2022).
65. Zhang, X. & Wei, S.-H. Origin of efficiency enhancement by lattice expansion in hybrid-perovskite solar cells. *Phys. Rev. Lett.* **128**, 136401 (2022).
66. Zhang, X., Turiansky, M. E., Shen, J.-X. & Van de Walle, C. G. Iodine interstitials as a cause of nonradiative recombination in hybrid perovskites. *Phys. Rev. B* **101**, 140101 (2020).
67. Zhang, X., Shen, J. X., Turiansky, M. E. & Van de Walle, C. G. Minimizing hydrogen vacancies to enable highly efficient hybrid perovskites. *Nat. Mater.* **20**, 971–976 (2021).
68. Whalley, L. D. Steric engineering of point defects in lead halide perovskites. *J. Phys. Chem. C* **127**, 15738–15746 (2023).
69. Wang, Y. et al. Octahedral tilting on halide perovskites. *Nat. Rev. Chem.* https://doi.org/10.1038/s41570-025-00687-6 (2025).
70. Stoumpos, C. C., Malliakas, C. D. & Kanatzidis, M. G. Semiconducting tin and lead iodide perovskites with organic cations: phase transitions, high mobilities, and near-infrared photoluminescent properties. *Inorg. Chem.* **52**, 9019–9038 (2013).
71. Mitzi, D. B., Feild, C. A., Schlesinger, Z. & Laibowitz, R. B. Transport, optical, and magnetic properties of the conducting halide perovskite $CH_3NH_3SnI_3$. *J. Solid State Chem.* **114**, 159–163 (1995).
72. Aharon, S., Gamliel, S., Cohen, B. E. & Etgar, L. Depletion region effect of highly efficient hole conductor free $CH_3NH_3PbI_3$ perovskite solar cells. *Phys. Chem. Chem. Phys.* **16**, 10512–10518 (2014).
73. Kirchartz, T., Bisquert, J., Mora-Sero, I. & Garcia-Belmonte, G. Classification of solar cells according to mechanisms of charge separation and charge collection. *Phys. Chem. Chem. Phys.* **17**, 4007–4014 (2015).
74. Walsh, A., Scanlon, D. O., Chen, S., Gong, X. G. & Wei, S.-H. Self-regulation mechanism for charged point defects in hybrid halide perovskites. *Angew. Chem.* **127**, 1811–1814 (2015).
75. Yang, J.-H., Yin, W.-J., Park, J.-S. & Wei, S.-H. Self-regulation of charged defect compensation and formation energy pinning in semiconductors. *Sci. Rep.* **5**, 16977 (2015).
76. Zhu, H. et al. Screening in crystalline liquids protects energetic carriers in hybrid perovskites. *Science* **353**, 1409–1413 (2016).
77. Miyata, K. et al. Large polarons in lead halide perovskites. *Sci. Adv.* **3**, e1701217 (2017).
78. Miyata, K. & Zhu, X.-Y. Ferroelectric large polarons. *Nat. Mater.* **17**, 379–381 (2018).
79. Wang, C. et al. Self-healing behavior of the metal halide perovskites and photovoltaics. *Small* **20**, 2307645 (2024).
80. Zhu, X.-Y. & Podzorov, V. Charge carriers in hybrid organic–inorganic lead halide perovskites might be protected as large polarons. *J. Phys. Chem. Lett.* **6**, 4758–4761 (2015).
81. Herz, L. M. Charge-carrier mobilities in metal halide perovskites: fundamental mechanisms and limits. *ACS Energy Lett.* **2**, 1539–1548 (2017).
82. Stranks, S. D. et al. Electron-hole diffusion lengths exceeding 1 micrometer in an organometal trihalide perovskite absorber. *Science* **342**, 341–344 (2013).
83. Chu, W., Zheng, Q., Prezhdo, O. V., Zhao, J. & Saidi, W. A. Low-frequency lattice phonons in halide perovskites explain high defect tolerance toward electron-hole recombination. *Sci. Adv.* **6**, eaaw7453 (2020).
84. Chu, W., Saidi, W. A., Zhao, J. & Prezhdo, O. V. Soft lattice and defect covalency rationalize tolerance of β-$CsPbI_3$ perovskite solar cells to native defects. *Angew. Chem. Int. Ed.* **59**, 6435–6441 (2020).
85. Spina, M. et al. Mechanical signatures of degradation of the photovoltaic perovskite $CH_3NH_3PbI_3$ upon water vapor exposure. *Appl. Phys. Lett.* **110**, 121903 (2017).
86. Fukuhara, M. & Yamauchi, I. Temperature dependence of the elastic moduli, dilational and shear internal frictions and acoustic wave velocity for alumina, (Y)TZP and β′-sialon ceramics. *J. Mater. Sci.* **28**, 4681–4688 (1993).
87. Leguy, A. M. A. et al. Dynamic disorder, phonon lifetimes, and the assignment of modes to the vibrational spectra of methylammonium lead halide perovskites. *Phys. Chem. Chem. Phys.* **18**, 27051–27066 (2016).
88. Frost, J. M. Calculating polaron mobility in halide perovskites. *Phys. Rev. B* **96**, 195202 (2017).
89. Kirchartz, T., Markvart, T., Rau, U. & Egger, D. A. Impact of small phonon energies on the charge-carrier lifetimes in metal-halide perovskites. *J. Phys. Chem. Lett.* **9**, 939–946 (2018).
90. Wang, S. et al. Effective lifetime of non-equilibrium carriers in semiconductors from non-adiabatic molecular dynamics simulations. *Nat. Comput. Sci.* **2**, 486–493 (2022).
91. Mukhuti, K., Sinha, S., Sinha, S. & Bansal, B. Dissipation-induced symmetry breaking: emphanitic transitions in lead- and tin-containing chalcogenides and halide perovskites. *Appl. Phys. Lett.* **118**, 162111 (2021).
92. Laurita, G., Fabini, D. H., Stoumpos, C. C., Kanatzidis, M. G. & Seshadri, R. Chemical tuning of dynamic cation off-centering in the cubic phases of hybrid tin and lead halide perovskites. *Chem. Sci.* **8**, 5628–5635 (2017).
93. Jensen, K. M. Ø. et al. Lattice dynamics reveals a local symmetry breaking in the emergent dipole phase of PbTe. *Phys. Rev. B* **86**, 085313 (2012).
94. Dubajic, M. et al. Dynamic nanodomains dictate macroscopic properties in lead halide perovskites. Preprint at https://doi.org/10.48550/ARXIV.2404.14598 (2024).
95. Walsh, A., Payne, D. J., Egdell, R. G. & Watson, G. W. Stereochemistry of post-transition metal oxides: revision of the classical lone pair model. *Chem. Soc. Rev.* **40**, 4455–4463 (2011).
96. Lang, F. et al. Radiation hardness and self-healing of perovskite solar cells. *Adv. Mater.* **28**, 8726–8731 (2016).
97. Andričević, P. et al. Kilogram-scale crystallogenesis of halide perovskites for gamma-rays dose rate measurements. *Adv. Sci.* **8**, 2001882 (2021).
98. Wei, H. et al. Sensitive X-ray detectors made of methylammonium lead tribromide perovskite single crystals. *Nat. Photonics* **10**, 333–339 (2016).
99. Domanski, K. et al. Migration of cations induces reversible performance losses over day/night cycling in perovskite solar cells. *Energy Environ. Sci.* **10**, 604–613 (2017).
100. Bag, M. et al. Kinetics of ion transport in perovskite active layers and its implications for active layer stability. *J. Am. Chem. Soc.* **137**, 13130–13137 (2015).
101. Nie, W. et al. Light-activated photocurrent degradation and self-healing in perovskite solar cells. *Nat. Commun.* **7**, 11574 (2016).
102. Yadav, P., Prochowicz, D., Alharbi, E. A., Zakeeruddin, S. M. & Grätzel, M. Intrinsic and interfacial kinetics of perovskite solar cells under photo and bias-induced degradation and recovery. *J. Mater. Chem. C* **5**, 7799–7805 (2017).
103. Yadavalli, S. K., Dai, Z., Zhou, H., Zhou, Y. & Padture, N. P. Facile healing of cracks in organic–inorganic halide perovskite thin films. *Acta Mater.* **187**, 112–121 (2020).
104. Al-Handawi, M. B. et al. Autonomous reconstitution of fractured hybrid perovskite single crystals. *Adv. Mater.* **34**, 2109374 (2022).
105. Guillemoles, J.-F., Rau, U., Kronik, L., Schock, H.-W. & Cahen, D. Cu(In,Ga)Se_2 solar cells: device stability based on chemical flexibility. *Adv. Mater.* **11**, 957–961 (1999).
106. Rakita, Y., Lubomirsky, I. & Cahen, D. When defects become 'dynamic': halide perovskites: a new window on materials? *Mater. Horiz.* **6**, 1297–1305 (2019).
107. Zhou, Z. et al. Methylamine-gas-induced defect-healing behavior of $CH_3NH_3PbI_3$ thin films for perovskite solar cells. *Angew. Chem. Int. Ed.* **54**, 9705–9709 (2015).
108. Hoye, R. L. Z. et al. The role of dimensionality on the optoelectronic properties of oxide and halide perovskites, and their halide derivatives. *Adv. Energy Mater.* **12**, 2100499 (2022).
109. Dunlap-Shohl, W. A., Hill, I. G., Yan, Y. & Mitzi, D. B. Photovoltaic effect in indium(I) iodide thin films. *Chem. Mater.* **30**, 8226–8232 (2018).
110. López-Fernández, I. et al. Lead-free halide perovskite materials and optoelectronic devices: progress and prospective. *Adv. Funct. Mater.* **34**, 2307896 (2024).
111. Ganose, A. M., Savory, C. N. & Scanlon, D. O. Beyond methylammonium lead iodide: prospects for the emergent field of ns^2 containing solar absorbers. *Chem. Commun.* **53**, 20–44 (2017).
112. Glück, N. & Bein, T. Prospects of lead-free perovskite-inspired materials for photovoltaic applications. *Energy Environ. Sci.* **13**, 4691–4716 (2020).
113. Ke, W. et al. Enhanced photovoltaic performance and stability with a new type of hollow 3D perovskite {en}$FASnI_3$. *Sci. Adv.* **3**, e1701293 (2017).
114. Lee, S. J. et al. Fabrication of efficient formamidinium tin iodide perovskite solar cells through SnF_2–pyrazine complex. *J. Am. Chem. Soc.* **138**, 3974–3977 (2016).
115. Koh, T. M. et al. Formamidinium tin-based perovskite with low E_g for photovoltaic applications. *J. Mater. Chem. A* **3**, 14996–15000 (2015).
116. Yu, B. et al. Heterogeneous 2D/3D tin-halides perovskite solar cells with certified conversion efficiency breaking 14%. *Adv. Mater.* **33**, 2102055 (2021).
117. Shao, S. et al. Highly reproducible Sn-based hybrid perovskite solar cells with 9% efficiency. *Adv. Energy Mater.* **8**, 1702019 (2018).
118. Dixit, H., Punetha, D. & Pandey, S. K. Improvement in performance of lead free inverted perovskite solar cell by optimization of solar parameters. *Optik* **179**, 969–976 (2019).
119. Shi, Y., Zhu, Z., Miao, D., Ding, Y. & Mi, Q. Interfacial dipoles boost open-circuit voltage of tin halide perovskite solar cells. *ACS Energy Lett.* **9**, 1895–1897 (2024).
120. Cui, D. et al. Making room for growing oriented $FASnI_3$ with large grains via cold precursor solution. *Adv. Funct. Mater.* **31**, 2100931 (2021).
121. Wang, C. et al. Self-repairing tin-based perovskite solar cells with a breakthrough efficiency over 11%. *Adv. Mater.* **32**, 1907623 (2020).
122. Meng, X. et al. Surface-controlled oriented growth of $FASnI_3$ crystals for efficient lead-free perovskite solar cells. *Joule* **4**, 902–912 (2020).
123. Ke, W. et al. TiO_2–ZnS cascade electron transport layer for efficient formamidinium tin iodide perovskite solar cells. *J. Am. Chem. Soc.* **138**, 14998–15003 (2016).
124. Li, F. et al. A cation-exchange approach for the fabrication of efficient methylammonium tin iodide perovskite solar cells. *Angew. Chem. Int. Ed.* **58**, 6688–6692 (2019).
125. Xu, F., Wei, H. & Cao, B. A hot phonon bottleneck observed upon incorporation of SnF_2 to $MASnI_3$ films and its possible role in increasing photocarrier diffusion length. *J. Appl. Phys.* **135**, 133102 (2024).
126. Ke, W. et al. Efficient lead-free solar cells based on hollow {en}$MASnI_3$ perovskites. *J. Am. Chem. Soc.* **139**, 14800–14806 (2017).

127. Ji, L. et al. Regulating crystallization dynamics and crystal orientation of methylammonium tin iodide enables high-efficiency lead-free perovskite solar cells. *Nanoscale* **14**, 1219–1225 (2022).
128. Ye, T. et al. Ambient-air-stable lead-free $CsSnI_3$ solar cells with greater than 7.5% efficiency. *J. Am. Chem. Soc.* **143**, 4319–4328 (2021).
129. Wang, Y. et al. Convenient preparation of $CsSnI_3$ quantum dots, excellent stability, and the highest performance of lead-free inorganic perovskite solar cells so far. *J. Mater. Chem. A* **7**, 7683–7690 (2019).
130. Marshall, K. P., Walker, M., Walton, R. I. & Hatton, R. A. Enhanced stability and efficiency in hole-transport-layer-free $CsSnI_3$ perovskite photovoltaics. *Nat. Energy* **1**, 16178 (2016).
131. Ye, T. et al. Localized electron density engineering for stabilized B-γ $CsSnI_3$-based perovskite solar cells with efficiencies >10%. *ACS Energy Lett.* **6**, 1480–1489 (2021).
132. Zhang, W. et al. Organic-free and lead-free perovskite solar cells with efficiency over 11%. *Adv. Energy Mater.* **12**, 2202491 (2022).
133. Song, T.-B., Yokoyama, T., Aramaki, S. & Kanatzidis, M. G. Performance enhancement of lead-free tin-based perovskite solar cells with reducing atmosphere-assisted dispersible additive. *ACS Energy Lett.* **2**, 897–903 (2017).
134. Dai, L. et al. Single-crystal nanowire cesium tin triiodide perovskite solar cell. *Small* **19**, 2208062 (2023).
135. Zhang, Z. et al. Over 12% efficient $CsSnI_3$ perovskite solar cells enabled by surface post-treatment with bi-functional polar molecules. *Chem. Eng. J.* **490**, 151561 (2024).
136. Cao, J. & Yan, F. Recent progress in tin-based perovskite solar cells. *Energy Environ. Sci.* **14**, 1286–1325 (2021).
137. Tai, Q. et al. Antioxidant grain passivation for air-stable tin-based perovskite solar cells. *Angew. Chem. Int. Ed.* **58**, 806–810 (2019).
138. Hasan, S. A. U., Lee, D. S., Im, S. H. & Hong, K.-H. Present status and research prospects of tin-based perovskite solar cells. *Sol. RRL* **4**, 1900310 (2020).
139. Krishnamoorthy, T. et al. Lead-free germanium iodide perovskite materials for photovoltaic applications. *J. Mater. Chem. A* **3**, 23829–23832 (2015).
140. Chiara, R., Morana, M. & Malavasi, L. Germanium-based halide perovskites: materials, properties, and applications. *ChemPlusChem* **86**, 879–888 (2021).
141. Mohan, R. Green bismuth. *Nat. Chem.* **2**, 336 (2010).
142. Park, B. et al. Bismuth based hybrid perovskites $A_3Bi_2I_9$ (A: methylammonium or cesium) for solar cell application. *Adv. Mater.* **27**, 6806–6813 (2015).
143. Bai, F. et al. Lead-free, air-stable ultrathin $Cs_3Bi_2I_9$ perovskite nanosheets for solar cells. *Sol. Energy Mater. Sol. Cells* **184**, 15–21 (2018).
144. Huang, P.-C., Yang, W.-C. & Lee, M.-W. $AgBiS_2$ semiconductor-sensitized solar cells. *J. Phys. Chem. C* **117**, 18308–18314 (2013).
145. Burgués-Ceballos, I., Wang, Y., Akgul, M. Z. & Konstantatos, G. Colloidal $AgBiS_2$ nanocrystals with reduced recombination yield 6.4% power conversion efficiency in solution-processed solar cells. *Nano Energy* **75**, 104961 (2020).
146. Zhou, S. et al. Preparation and photovoltaic properties of ternary $AgBiS_2$ quantum dots sensitized TiO_2 nanorods photoanodes by electrochemical atomic layer deposition. *J. Electrochem. Soc.* **163**, D63–D67 (2016).
147. Bernechea, M. et al. Solution-processed solar cells based on environmentally friendly $AgBiS_2$ nanocrystals. *Nat. Photonics* **10**, 521–525 (2016).
148. Li, X. et al. Thin film $AgBiS_2$ solar cells with over 10% power conversion efficiency enabled by vapor-assisted solution process treatment. *Chem. Eng. J.* **495**, 153328 (2024).
149. Sfaelou, S., Raptis, D., Dracopoulos, V. & Lianos, P. BiOI solar cells. *RSC Adv.* **5**, 95813–95816 (2015).
150. Wang, K., Jia, F., Zheng, Z. & Zhang, L. Crossed BiOI flake array solar cells. *Electrochem. Commun.* **12**, 1764–1767 (2010).
151. Jain, S. M. et al. An effective approach of vapour assisted morphological tailoring for reducing metal defect sites in lead-free, $(CH_3NH_3)_3Bi_2I_9$ bismuth-based perovskite solar cells for improved performance and long-term stability. *Nano Energy* **49**, 614–624 (2018).
152. Huang, Y.-T. et al. Strong absorption and ultrafast localisation in $NaBiS_2$ nanocrystals with slow charge-carrier recombination. *Nat. Commun.* **13**, 4960 (2022).
153. Lal, S. et al. The role of chemical composition in determining the charge-carrier dynamics in $(AgI)_x(BiI_3)_y$ rudorffites. *Adv. Funct. Mater.* **34**, 2315942 (2024).
154. Jia, Z. et al. Charge-carrier dynamics of solution-processed antimony- and bismuth-based chalcogenide thin films. *ACS Energy Lett.* **8**, 1485–1492 (2023).
155. Lal, S. et al. Bandlike transport and charge-carrier dynamics in BiOI films. *J. Phys. Chem. Lett.* **14**, 6620–6629 (2023).
156. Wang, Y. et al. Cation disorder engineering yields $AgBiS_2$ nanocrystals with enhanced optical absorption for efficient ultrathin solar cells. *Nat. Photonics* **16**, 235–241 (2022).
157. Septina, W., Ikeda, S., Iga, Y., Harada, T. & Matsumura, M. Thin film solar cell based on $CuSbS_2$ absorber fabricated from an electrochemically deposited metal stack. *Thin Solid Films* **550**, 700–704 (2014).
158. Li, Z. et al. 9.2%-efficient core-shell structured antimony selenide nanorod array solar cells. *Nat. Commun.* **10**, 125 (2019).
159. Kolay, A. et al. New antimony selenide/nickel oxide photocathode boosts the efficiency of graphene quantum-dot co-sensitized solar cells. *ACS Appl. Mater. Interfaces* **9**, 34915–34926 (2017).
160. Choi, Y. C. et al. Sb_2Se_3-sensitized inorganic–organic heterojunction solar cells fabricated using a single-source precursor. *Angew. Chem. Int. Ed.* **53**, 1329–1333 (2014).
161. Duan, Z. et al. Sb_2Se_3 thin-film solar cells exceeding 10% power conversion efficiency enabled by injection vapor deposition technology. *Adv. Mater.* **34**, 2202969 (2022).
162. Leng, M. et al. Selenization of Sb_2Se_3 absorber layer: an efficient step to improve device performance of CdS/Sb_2Se_3 solar cells. *Appl. Phys. Lett.* **105**, 083905 (2014).
163. Zhou, Y. et al. Thin-film Sb_2Se_3 photovoltaics with oriented one-dimensional ribbons and benign grain boundaries. *Nat. Photonics* **9**, 409–415 (2015).
164. Wang, S. et al. A novel multi-sulfur source collaborative chemical bath deposition technology enables 8%-efficiency Sb_2S_3 planar solar cells. *Adv. Mater.* **34**, 2206242 (2022).
165. Chang, J. A. et al. High-performance nanostructured inorganic–organic heterojunction solar cells. *Nano Lett.* **10**, 2609–2612 (2010).
166. Choi, Y. C., Lee, D. U., Noh, J. H., Kim, E. K. & Seok, S. I. Highly improved Sb_2S_3 sensitized-inorganic–organic heterojunction solar cells and quantification of traps by deep-level transient spectroscopy. *Adv. Funct. Mater.* **24**, 3587–3592 (2014).
167. Nezu, S. et al. Light soaking and gas effect on nanocrystalline TiO_2/Sb_2S_3/CuSCN photovoltaic cells following extremely thin absorber concept. *J. Phys. Chem. C* **114**, 6854–6859 (2010).
168. Chang, J. A. et al. Panchromatic photon-harvesting by hole-conducting materials in inorganic–organic heterojunction sensitized-solar cell through the formation of nanostructured electron channels. *Nano Lett.* **12**, 1863–1867 (2012).
169. Itzhaik, Y., Niitsoo, O., Page, M. & Hodes, G. Sb_2S_3-sensitized nanoporous TiO_2 solar cells. *J. Phys. Chem. C* **113**, 4254–4256 (2009).
170. Im, S. H. et al. Toward interaction of sensitizer and functional moieties in hole-transporting materials for efficient semiconductor-sensitized solar cells. *Nano Lett.* **11**, 4789–4793 (2011).
171. Chen, X. et al. Solvent-assisted hydrothermal deposition approach for highly-efficient $Sb_2(S,Se)_3$ thin-film solar cells. *Adv. Energy Mater.* **13**, 2300391 (2023).
172. Messina, S., Nair, M. T. S. & Nair, P. K. Antimony selenide absorber thin films in all-chemically deposited solar cells. *J. Electrochem. Soc.* **156**, H327 (2009).
173. Choi, Y. C. et al. Efficient inorganic-organic heterojunction solar cells employing $Sb_2(S_x/Se_{1-x})_3$ graded-composition sensitizers. *Adv. Energy Mater.* **4**, 1301680 (2014).
174. Tang, R. et al. Hydrothermal deposition of antimony selenosulfide thin films enables solar cells with 10% efficiency. *Nat. Energy* **5**, 587–595 (2020).
175. Wu, C. et al. Interfacial engineering by indium-doped CdS for high efficiency solution processed $Sb_2(S_{1-x}Se_x)_3$ solar cells. *ACS Appl. Mater. Interfaces* **11**, 3207–3213 (2019).
176. Wang, X. et al. Manipulating the electrical properties of $Sb_2(S,Se)_3$ film for high-efficiency solar cell. *Adv. Energy Mater.* **10**, 2002341 (2020).
177. Zhao, Y. et al. Regulating energy band alignment via alkaline metal fluoride assisted solution post-treatment enabling $Sb_2(S,Se)_3$ solar cells with 10.7% efficiency. *Adv. Energy Mater.* **12**, 2103015 (2022).
178. Zhao, Y. et al. Regulating deposition kinetics via a novel additive-assisted chemical bath deposition technology enables fabrication of 10.57%-efficiency Sb_2Se_3 solar cells. *Energy Environ. Sci.* **15**, 5118–5128 (2022).
179. Liu, X. et al. Grain engineering of Sb_2S_3 thin films to enable efficient planar solar cells with high open-circuit voltage. *Adv. Mater.* **36**, 2305841 (2024).
180. Chen, X. et al. Additive engineering for Sb_2S_3 indoor photovoltaics with efficiency exceeding 17%. *Light Sci. Appl.* **13**, 281 (2024).
181. Welch, A. W. et al. $CuSbSe_2$ photovoltaic devices with 3% efficiency. *Appl. Phys. Express* **8**, 082301 (2015).
182. Welch, A. W. et al. Trade-offs in thin film solar cells with layered chalcostibite photovoltaic absorbers. *Adv. Energy Mater.* **7**, 1601935 (2017).
183. Banu, S., Ahn, S. J., Ahn, S. K., Yoon, K. & Cho, A. Fabrication and characterization of cost-efficient $CuSbS_2$ thin film solar cells using hybrid inks. *Sol. Energy Mater. Sol. Cells* **151**, 14–23 (2016).
184. Correa-Baena, J.-P. et al. *A*-site cation in inorganic $A_3Sb_2I_9$ perovskite influences structural dimensionality, exciton binding energy, and solar cell performance. *Chem. Mater.* **30**, 3734–3742 (2018).
185. Singh, A. et al. Panchromatic heterojunction solar cells for Pb-free all-inorganic antimony based perovskite. *Chem. Eng. J.* **419**, 129424 (2021).
186. Singh, A. et al. Photovoltaic performance of vapor-assisted solution-processed layer polymorph of $Cs_3Sb_2I_9$. *ACS Appl. Mater. Interfaces* **10**, 2566–2573 (2018).
187. Yang, B. et al. $CuSbS_2$ as a promising earth-abundant photovoltaic absorber material: a combined theoretical and experimental study. *Chem. Mater.* **26**, 3135–3143 (2014).
188. Peccerillo, E. & Durose, K. Copper—antimony and copper—bismuth chalcogenides—Research opportunities and review for solar photovoltaics. *MRS Energy Sustain.* **5**, 9 (2018).
189. Yee, Y. S. et al. Copper interstitial recombination centers in Cu_3N. *Phys. Rev. B* **97**, 245201 (2018).
190. Kurchin, R. C., Gorai, P., Buonassisi, T. & Stevanović, V. Structural and chemical features giving rise to defect tolerance of binary semiconductors. *Chem. Mater.* **30**, 5583–5592 (2018).
191. Huq, T. N. et al. Electronic structure and optoelectronic properties of bismuth oxyiodide robust against percent-level iodine-, oxygen-, and bismuth-related surface defects. *Adv. Funct. Mater.* **30**, 1909983 (2020).
192. Hoye, R. L. Z. et al. Strongly enhanced photovoltaic performance and defect physics of air-stable bismuth oxyiodide (BiOI). *Adv. Mater.* **29**, 1702176 (2017).
193. Shi, H. & Du, M.-H. Shallow halogen vacancies in halide optoelectronic materials. *Phys. Rev. B* **90**, 174103 (2014).
194. Pandey, M. et al. Defect-tolerant monolayer transition metal dichalcogenides. *Nano Lett.* **16**, 2234–2239 (2016).
195. Pecunia, V., Occhipinti, L. G. & Hoye, R. L. Z. Emerging indoor photovoltaic technologies for sustainable internet of things. *Adv. Energy Mater.* **11**, 2100698 (2021).
196. Bhattarai, S., Sharma, A. & Das, T. D. Efficiency enhancement of perovskite solar cell by using doubly carrier transport layers with a distinct bandgap of $MAPbI_3$ active layer. *Optik* **224**, 165430 (2020).

197. Zhao, X. et al. Macroscopic piezoelectricity of an $MAPbI_3$ semiconductor and its associated multifunctional device. *Nano Energy* **118**, 108980 (2023).
198. Savory, C. N. & Scanlon, D. O. The complex defect chemistry of antimony selenide. *J. Mater. Chem. A* **7**, 10739–10744 (2019).
199. Hobson, T. D. C., Phillips, L. J., Hutter, O. S., Durose, K. & Major, J. D. Defect properties of Sb_2Se_3 thin film solar cells and bulk crystals. *Appl. Phys. Lett.* **116**, 261101 (2020).
200. Wang, X., Kavanagh, S. R., Scanlon, D. O. & Walsh, A. Four-electron negative-*U* vacancy defects in antimony selenide. *Phys. Rev. B* **108**, 134102 (2023).
201. Franchini, C., Reticcioli, M., Setvin, M. & Diebold, U. Polarons in materials. *Nat. Rev. Mater.* **6**, 560–586 (2021).
202. Wright, A. D. et al. Ultrafast excited-state localization in $Cs_2AgBiBr_6$ double perovskite. *J. Phys. Chem. Lett.* **12**, 3352–3360 (2021).
203. McCall, K. M., Stoumpos, C. C., Kostina, S. S., Kanatzidis, M. G. & Wessels, B. W. Strong electron–phonon coupling and self-trapped excitons in the defect halide perovskites $A_3M_2I_9$ (A=Cs, Rb; M=Bi, Sb). *Chem. Mater.* **29**, 4129–4145 (2017).
204. Scholz, M., Oum, K. & Lenzer, T. Pronounced exciton and coherent phonon dynamics in BiI. *Phys. Chem. Chem. Phys.* **20**, 10677–10685 (2018).
205. Buizza, L. R. V. et al. Interplay of structure, charge-carrier localization and dynamics in copper-silver-bismuth-halide semiconductors. *Adv. Funct. Mater.* **32**, 2108392 (2022).
206. Fu, Y. et al. Structural and electronic features enabling delocalized charge-carriers in $CuSbSe_2$. *Nat Commun* **16**, 65 (2025).
207. Chen, Y.-T. et al. Interlayer quasi-bonding interactions in 2D layered materials: a classification according to the occupancy of involved energy bands. *J. Phys. Chem. Lett.* **12**, 11998–12004 (2021).
208. Jagt, R. A. et al. Layered BiOI single crystals capable of detecting low dose rates of X-rays. *Nat. Commun.* **14**, 2452 (2023).
209. Siekmann, J., Ravishankar, S. & Kirchartz, T. Apparent defect densities in halide perovskite thin films and single crystals. *ACS Energy Lett.* **6**, 3244–3251 (2021).
210. De Keersmaecker, M., Tirado, J., Armstrong, N. R. & Ratcliff, E. L. Defect quantification in metal halide perovskites anticipates photoluminescence and photovoltaic performance. *ACS Energy Lett.* **9**, 243–252 (2024).
211. Cahen, D., Rakita, Y., Egger, D. A. & Kahn, A. Surface defects control bulk carrier densities in polycrystalline Pb-halide perovskites. *Adv. Mater.* **36**, 2407098 (2024).
212. Reichert, S. et al. Probing the ionic defect landscape in halide perovskite solar cells. *Nat. Commun.* **11**, 6098 (2020).
213. Eames, C. et al. Ionic transport in hybrid lead iodide perovskite solar cells. *Nat. Commun.* **6**, 7497 (2015).
214. Huang, Y.-T. et al. Fast near-infrared photodetectors based on nontoxic and solution-processable $AgBiS_2$. *Small* **20**, 2310199 (2024).
215. Armaroli, G. et al. Photoinduced current transient spectroscopy on metal halide perovskites: electron trapping and ion drift. *ACS Energy Lett.* **8**, 4371–4379 (2023).
216. Ciavatti, A. et al. Radiation hardness and defects activity in PEA_2PbBr_4 single crystals. *Adv. Funct. Mater.* **34**, 2405291 (2024).
217. Zhu, Y. & Cheng, J.-X. Transient absorption microscopy: technological innovations and applications in materials science and life science. *J. Chem. Phys.* **152**, 020901 (2020).
218. Ke, D. et al. Ultrafast dynamics of defect-assisted carrier capture in MoS_2 nanodots investigated by transient absorption spectroscopy. *Chin. J. Chem. Phys.* **31**, 277–283 (2018).
219. Lo, S. S. et al. CdTe nanowires studied by transient absorption microscopy. *EPJ Web Conf.* **41**, 04032 (2013).
220. Nah, S. et al. Transient sub-bandgap states in halide perovskite thin films. *Nano Lett.* **18**, 827–831 (2018).
221. Snaider, J. M. et al. Ultrafast imaging of carrier transport across grain boundaries in hybrid perovskite thin films. *ACS Energy Lett.* **3**, 1402–1408 (2018).
222. Xie, J. et al. Visualizing carrier diffusion in Cs-doping $FAPbI_3$ perovskite thin films using transient absorption microscopy. *Adv. Opt. Mater.* **12**, 2303004 (2024).
223. Frohna, K. et al. Nanoscale chemical heterogeneity dominates the optoelectronic response of alloyed perovskite solar cells. *Nat. Nanotechnol.* **17**, 190–196 (2022).
224. Simpson, M. J., Doughty, B., Yang, B., Xiao, K. & Ma, Y.-Z. Imaging electronic trap states in perovskite thin films with combined fluorescence and femtosecond transient absorption microscopy. *J. Phys. Chem. Lett.* **7**, 1725–1731 (2016).
225. Lin, Y.-H. et al. Bandgap-universal passivation enables stable perovskite solar cells with low photovoltage loss. *Science* **384**, 767–775 (2024).
226. Stranks, S. D. Multimodal microscopy characterization of halide perovskite semiconductors: revealing a new world (dis)order. *Matter* **4**, 3852–3866 (2021).
227. Kosar, S. et al. Unraveling the varied nature and roles of defects in hybrid halide perovskites with time-resolved photoemission electron microscopy. *Energy Environ. Sci.* **14**, 6320–6328 (2021).
228. Doherty, T. A. S. et al. Performance-limiting nanoscale trap clusters at grain junctions in halide perovskites. *Nature* **580**, 360–366 (2020).
229. Kosar, S. & Dani, K. M. Time-resolved photoemission electron microscopy of semiconductor interfaces. *Prog. Surf. Sci.* **99**, 100745 (2024).
230. Ye, J. et al. Extending the defect tolerance of halide perovskite nanocrystals to hot carrier cooling dynamics. *Nat. Commun.* **15**, 8120 (2024).
231. Le Bris, A. et al. Hot carrier solar cells: controlling thermalization in ultrathin devices. *IEEE J. Photovolt.* **2**, 506–511 (2012).
232. Li, M., Fu, J., Xu, Q. & Sum, T. C. Slow hot-carrier cooling in halide perovskites: prospects for hot-carrier solar cells. *Adv. Mater.* **31**, 1802486 (2019).
233. Poindexter, J. R. et al. High tolerance to iron contamination in lead halide perovskite solar cells. *ACS Nano* **11**, 7101–7109 (2017).
234. Kim, S., Márquez, J. A., Unold, T. & Walsh, A. Upper limit to the photovoltaic efficiency of imperfect crystals from first principles. *Energy Environ. Sci.* **13**, 1481–1491 (2020).
235. Shockley, W. & Read, W. T. Statistics of the recombinations of holes and electrons. *Phys. Rev.* **87**, 835–842 (1952).
236. Stoneham, A. M. Non-radiative transitions in semiconductors. *Rep. Prog. Phys.* **44**, 1251 (1981).
237. Mosquera-Lois, I., Klarbring, J. & Walsh, A. Point defect formation at finite temperatures with machine learning force fields. Preprint at https://doi.org/10.48550/arXiv.2412.16741 (2024).
238. Park, J. S., Kim, S., Xie, Z. & Walsh, A. Point defect engineering in thin-film solar cells. *Nat. Rev. Mater.* **3**, 194–210 (2018).
239. Yang, J.-H., Yin, W.-J., Park, J.-S., Ma, J. & Wei, S.-H. Review on first-principles study of defect properties of CdTe as a solar cell absorber. *Semicond. Sci. Technol.* **31**, 083002 (2016).
240. Ma, J. et al. Dependence of the minority-carrier lifetime on the stoichiometry of CdTe using time-resolved photoluminescence and first-principles calculations. *Phys. Rev. Lett.* **111**, 067402 (2013).
241. Mosquera-Lois, I., Kavanagh, S. R., Walsh, A. & Scanlon, D. O. Identifying the ground state structures of point defects in solids. *npj Comput. Mater.* **9**, 25 (2023).
242. Mosquera-Lois, I. & Kavanagh, S. R. In search of hidden defects. *Matter* **4**, 2602–2605 (2021).
243. Mosquera-Lois, I., Kavanagh, S. R., Ganose, A. M. & Walsh, A. Machine-learning structural reconstructions for accelerated point defect calculations. *npj Comput. Mater.* **10**, 121 (2024).
244. Freysoldt, C. et al. First-principles calculations for point defects in solids. *Rev. Mod. Phys.* **86**, 253–305 (2014).
245. Mosquera-Lois, I., Kavanagh, S. R., Klarbring, J., Tolborg, K. & Walsh, A. Imperfections are not 0 K: free energy of point defects in crystals. *Chem. Soc. Rev.* **52**, 5812–5826 (2023).
246. Broberg, D. et al. PyCDT: a python toolkit for modeling point defects in semiconductors and insulators. *Comput. Phys. Commun.* **226**, 165–179 (2018).
247. Shen, J.-X. & Varley, J. pymatgen-analysis-defects: a python package for analyzing point defects in crystalline materials. *J. Open Source Softw.* **9**, 5941 (2024).
248. Squires, A. G., Scanlon, D. O. & Morgan, B. J. py-sc-fermi: self-consistent Fermi energies and defect concentrations from electronic structure calculations. *J. Open Source Softw.* **8**, 4962 (2023).
249. Mosquera-Lois, I., Kavanagh, S. R., Walsh, A. & Scanlon, D. O. ShakeNBreak: navigating the defect configurational landscape. *J. Open Source Softw.* **7**, 4817 (2022).
250. Neilson, W. D. & Murphy, S. T. DefAP: a Python code for the analysis of point defects in crystalline solids. *Comput. Mater. Sci.* **210**, 111434 (2022).
251. Goyal, A., Gorai, P., Peng, H., Lany, S. & Stevanović, V. A computational framework for automation of point defect calculations. *Comput. Mater. Sci.* **130**, 1–9 (2017).
252. Kavanagh, S. R. et al. doped: Python toolkit for robust and repeatable charged defect supercell calculations. *J. Open Source Softw.* **9**, 6433 (2024).
253. Kumagai, Y., Tsunoda, N., Takahashi, A. & Oba, F. Insights into oxygen vacancies from high-throughput first-principles calculations. *Phys. Rev. Mater.* **5**, 123803 (2021).
254. Zhang, X., Turiansky, M. E. & Van de Walle, C. G. Correctly assessing defect tolerance in halide perovskites. *J. Phys. Chem. C* **124**, 6022–6027 (2020).
255. Zhang, X., Shen, J.-X., Turiansky, M. E. & de Walle, C. G. V. Hidden role of Bi incorporation in nonradiative recombination in methylammonium lead iodide. *J. Mater. Chem. A* **8**, 12964–12967 (2020).
256. Shi, L. & Wang, L.-W. Ab initio calculations of deep-level carrier nonradiative recombination rates in bulk semiconductors. *Phys. Rev. Lett.* **109**, 245501 (2012).
257. Kim, S., Hood, S. N. & Walsh, A. Anharmonic lattice relaxation during nonradiative carrier capture. *Phys. Rev. B* **100**, 041202 (2019).
258. Kim, S., Hood, S. N., Gerwen, P., van, Whalley, L. D. & Walsh, A. CarrierCapture.jl: anharmonic carrier capture. *J. Open Source Softw.* **5**, 2102 (2020).
259. Turiansky, M. E. et al. Nonrad: computing nonradiative capture coefficients from first principles. *Comput. Phys. Commun.* **267**, 108056 (2021).
260. Qiao, L., Fang, W.-H., Long, R. & Prezhdo, O. V. Atomic model for alkali metal passivation of point defects at perovskite grain boundaries. *ACS Energy Lett.* **5**, 3813–3820 (2020).
261. Zhao, K., Xiang, H., Zhu, R., Liu, C. & Jia, Y. Passivation principle of deep-level defects: a study of SnZn defects in kesterites for high-efficient solar cells. *J. Mater. Chem. A* **10**, 2849–2855 (2022).
262. Cai, Z. et al. Active passivation of anion vacancies in antimony selenide film for efficient solar cells. *Adv. Mater.* **36**, 2404826 (2024).
263. Du, Y. et al. Defect engineering in earth-abundant $Cu_2ZnSn(S,Se)_4$ photovoltaic materials via Ga^{3+}-doping for over 12% efficient solar cells. *Adv. Funct. Mater.* **31**, 2010325 (2021).
264. de Mello, J. C., Wittmann, H. F. & Friend, R. H. An improved experimental determination of external photoluminescence quantum efficiency. *Adv. Mater.* **9**, 230–232 (1997).
265. Becker, W. in *Advanced Time-Correlated Single Photon Counting Applications* (ed. Becker, W.) 1–63 (Springer, 2015).
266. Berera, R., van Grondelle, R. & Kennis, J. T. M. Ultrafast transient absorption spectroscopy: principles and application to photosynthetic systems. *Photosynth. Res.* **101**, 105–118 (2009).
267. Guthrey, H. & Moseley, J. A review and perspective on cathodoluminescence analysis of halide perovskites. *Adv. Energy Mater.* **10**, 1903840 (2020).
268. Righetto, M. et al. Hot carriers perspective on the nature of traps in perovskites. *Nat. Commun.* **11**, 2712 (2020).

269. Pan, J. et al. Operando dynamics of trapped carriers in perovskite solar cells observed via infrared optical activation spectroscopy. *Nat. Commun.* **14**, 8000 (2023).
270. Sadhanala, A. et al. Preparation of single-phase films of $CH_3NH_3Pb(I_{1-x}Br_x)_3$ with sharp optical band edges. *J. Phys. Chem. Lett.* **5**, 2501–2505 (2014).
271. Kronik, L. & Shapira, Y. Surface photovoltage phenomena: theory, experiment, and applications. *Surf. Sci. Rep.* **37**, 1–206 (1999).
272. van Gorkom, B. T., van der Pol, T. P. A., Datta, K., Wienk, M. M. & Janssen, R. A. J. Revealing defective interfaces in perovskite solar cells from highly sensitive sub-bandgap photocurrent spectroscopy using optical cavities. *Nat. Commun.* **13**, 349 (2022).
273. Le Corre, V. M. et al. Revealing charge carrier mobility and defect densities in metal halide perovskites via space-charge-limited current measurements. *ACS Energy Lett.* **6**, 1087–1094 (2021).
274. Lang, D. V. Deep-level transient spectroscopy: a new method to characterize traps in semiconductors. *J. Appl. Phys.* **45**, 3023–3032 (1974).
275. Losee, D. L. Admittance spectroscopy of deep impurity levels: ZnTe Schottky barriers. *Appl. Phys. Lett.* **21**, 54–56 (1972).
276. Leon, C., Le Gall, S., Gueunier-Farret, M.-E. & Kleider, J.-P. How to perform admittance spectroscopy and DLTS in multijunction solar cells. *Sol. Energy Mater. Sol. Cells* **240**, 111699 (2022).
277. Bollmann, J. & Venter, A. Admittance spectroscopy or deep level transient spectroscopy: a contrasting juxtaposition. *Phys. B* **535**, 237–241 (2018).

Acknowledgements

Y.-T.H. and H.L. arranged alphabetically by surname in the author list. I.M.-L. acknowledges Imperial College London for funding from a President's PhD scholarship. R.L.Z.H., H.L. and J.Y. acknowledge support from a UK Research and Innovation Frontier Grant (grant no. EP/X029900/1), awarded through the European Research Council Starting Grant 2021 scheme. H.L. thanks the Department of Chemistry at the University of Oxford for a studentship. R.L.Z.H. and Y.-T.H. thank the Engineering and Physical Sciences Research Council (EPSRC, grant no. EP/V014498/2) for financial support. A.W. is supported by EPSRC project no. EP/X037754/1. R.L.Z.H. thanks the Royal Academy of Engineering and Science & Technology Facilities Council for financial support through the Senior Research Fellowships scheme (grant no. RCSRF2324-18-68).

Author contributions

R.L.Z.H. and A.W. conceived of the idea for this Review and drafted the proposal, with support from the other authors. R.L.Z.H. wrote the introduction, Box 1 and Box 3, the Defining defect tolerance section, drafted the Conclusions and outlook, contributed to Fig. 1, and prepared Fig. 5. I.M.-L. and A.W. wrote the models for defect tolerance in LHPs, prepared Box 2, and contributed to Figs. 1 and 2. J.Y. wrote the Polaronic model sub-section in the main discussion and outlook section, contributed to Fig. 2, and also wrote the section on defect characterization with R.L.Z.H. H.L. prepared Fig. 3, and the discussion around it, whereas Y.-T.H. prepared Fig. 4 and the associated discussion. All authors edited and revised the manuscript.

Competing interests

The authors declare no competing interests.

Additional information

Supplementary information The online version contains supplementary material available at https://doi.org/10.1038/s41570-025-00702-w.

Peer review information *Nature Reviews Chemistry* thanks the anonymous reviewers for their contribution to the peer review of this work.